Towards an all-printed biodegradable battery

SUPPORTING INFORMATION

Alexis Laforgue[1], Asmae Mokrini[1], Edmond Lam[2], Alfred Chi Woon Leung[2], Yali Liu[2], Sophie Régnier[2], Denis Rho[2], Marie-Josée Lorrain[2], Robert Black[3], Andrew Wang[3], Nathalie Chapleau[4], Naveen Chopra[5], Gregory McGuire[5] and Nan-Xing Hu[5]

[1] National Research Council Canada, Clean Energy Innovation Research Centre, 75 de Mortagne Boulevard, Boucherville, Québec, J4B 6Y4, Canada

[2] National Research Council Canada, Aquatic and Crop Resource Development Research Centre, 6100 Royalmount Avenue, Montreal, Québec, H4P 2R2, Canada

[3] National Research Council Canada, Clean Energy Innovation Research Centre, 2620 Speakman Drive, Mississauga, Ontario, L5K 1B1, Canada

[4] National Research Council Canada, Automotive and Surface Transportation Research Centre, 75 de Mortagne Boulevard, Boucherville, Québec, J4B 6Y4, Canada

[5] Xerox Research Centre of Canada, 2660 Speakman Drive, Mississauga, Ontario, L5K 2L1, Canada

SECTION 1: BATTERY DESIGN ……. p. 2

SECTION 2: SUBSTRATE AND PACKAGING ……. p. 6

SECTION 3: ELECTRODE BINDERS ……..p. 12

SECTION 4: GEL POLYMER ELECTROLYTE .....p. 19

SECTION 5: BATTERY PRINTING AND ASSEMBLY ……. p. 38

SECTION 6: PERFORMANCE TESTING ……. p. 42

SECTION 7: COMPOSTABILITY TESTING ……. p. 46

SECTION 1: BATTERY DESIGN

Discussion on the biodegradation vs. recycling of printed batteries

The environmental sustainability of a product can be achieved either through its biodegradation (cradle-to-grave) or recycling processes (cradle-to-cradle). Each end-of-life strategy has its own merits and drawbacks, and the choice to favor one or the other depends on many parameters.

Recycling a product allows the re-use of its components to fabricate new products (ideally the same ones), which leads to a virtuous circular economy. However, it can be a complicated process, especially for multi-component devices such as batteries, potentially implying multiple steps of disassembly, component separation and recovery of selected materials. Moreover, to recover the metallic components (usually the most valuable ones), energy-intensive and costly processes are typically employed, such as pyrometallurgy or hydrometallurgy [1]. Therefore, the economic viability of recycling processes depends on the relative values of the materials to be recovered. It can be interesting to look at the case of primary alkaline batteries: the energy cost to recover Zn and Mn is 6 to 10 times higher than to extract and refine the metals from the ore, which limits the economical incentive to develop a proper recycling industry, even though the potential gains in terms of energy savings and CO_2 footprint reduction would be significant [2].

On the other hand, the biodegradation route does not require specific economical incentives, since the products can be processed through an already well established industrial process (municipal composting facilities, when available), or simply let to degrade using natural processes, which are less efficient but do not lead to environmental poisoning. Another significant advantage of composting a product is the low energy required, making it a quite efficient process. The biodegradation strategy can be particularly interesting for multi-component devices such as batteries, since it does not require the disassembly and separation of materials, significantly simplifying the process and decreasing the associated costs. The challenges related to this strategy rather lie at the design and fabrication stages, where all components have to be made of biodegradable materials, and should not release environmentally toxic byproducts, which is far from being obvious, as shown by the results of this work. The biodegradation route also disseminates the materials in the soil instead of recovering them, which prevents their further re-use for the fabrication of new products.

Ultimately, establishing the best strategy requires an exhaustive analysis for each product, taking into account multiple factors both technical and economical. The most important part is to embed a sustainable end-of-life strategy at the core of the design of new products, allowing to develop a globally more sustainable economy.

Discussion on the safety aspects of composting batteries

One important aspect to consider for compostable batteries is the impact on the safety of the composting process. It is known that flammable gases can be generated by specific anaerobic composting processes (without oxygen), which usually produce methane or biogas (a mix of methane and carbon dioxide). However, the process typically used by industrial composters (in particular in municipalities) is an aerobic process, supposed to generate only carbon dioxide and water vapour. The safety concern with aerobic composting is overheating, which can occur when the decomposition of organic matters is not properly monitored, and can lead to the uncontrolled combustion of the compost pile and ultimately pile fires [3]. This unsafe situation is generally avoided quite simply by monitoring the temperature of the pile and regularly aerating it through mechanical mixing, thus preventing the buildup of gases and temperature.

A possible risk of adding biodegradable batteries to a compost pile is the generation of self-heating (by external or internal short-circuit of the batteries) that could lead to compost pile fire. However, Zn-MnO_2 batteries, such as the one developed in this study, are inherently safe since they use non-flammable aqueous electrolytes. A recent study showed that the temperature onset of thermal runaway for alkaline Zn-MnO_2 batteries (290-380 °C) is much higher than that of Li-ion batteries. Such a temperature level that is never found in a compost pile [4]. Moreover, potential short-circuits in composted Zn-MnO_2 batteries are not believed to generate sufficient self-heating to lead to compost combustion. Indeed, no specific self-heating was observed in the composting tests of this study, even though a high number of batteries were placed in each reactor (see SI section 7, p. 46). This, however, would need to be confirmed by larger scale experiments and remains an important point to address for the safe management of compostable batteries.

Ref.	Year	Chemistry anode/electrolyte/cathode	Operating voltage	Performances	Design and manufacturing	Biodegradation conditions
5	2014	Mg / PBS / Mo (ORR)	0.45 V	1.2 mWh/cm² at 50 µW/cm²	Open cell (Mg-air chemistry); bulky design using UV curing of polyanhydride casing in PDMS molds; manual layer-by-layer assembly; no clear potential for scale-up.	Dissolution in PBS at 85 °C in 19 days.
6	2021	Pyroprotein carbon / $NaClO_4$ in PC / $Na_4Fe_3(PO_4)_2(P_2O_7)$	2.5 V	0.3 mWh/cm² at 0.4 mW/cm², rechargeable	Na-ion chemistry with an organic electrolyte; active layers printed on substrates; Manual cell assembly, but compatible with Li-ion production methods; needs a dry environment for cell assembly (anhydrous organic electrolyte).	Partial degradation after 120 days when buried in plant soil.
7	2022	Zn / NaCl / Graphite (ORR)	0.5 V	75 µWh/cm² at 50 µW/cm² until battery drying	Open cell (Zn-air chemistry); active layers printed on a cellulosic paper impregnated with beewax for patterning purposes; has to be activated by water; no clear potential for scale-up.	Biodegradability not assessed.
8	2022	Mg / 0.5 M $CaCl_2$ in PBS / MoO_3	1.0 V	1.7 mWh/cm² at 45 µW/cm²	Stretchable design obtained by laser-cutting of electrode/separator; manual layer-by-layer assembly; no clear potential for scale-up.	Dissolution in PBS at 85 °C in 73 days.
9	2022	Zn / $ZnCl_2$+$ZnSO_4$+$MnSO_4$ in H_2O / MnO_2	1.35 V	1.5 mWh/cm² at 1.3 mW/cm², rechargeable	Thin printed layers: electrodes printed on each side of a PAAM-filled paper separator + gold current collector layers evaporated on each electrode; reasonably good potential for scale-up, but production time of PAAM-filled separator needs to be reduced drastically.	Degradation of PAAM-filled cellulose separator only: complete degradation after 28 days when buried in garden soil.
9	2022	Zn / KOH+LiOH in H_2O / $Ni(OH)_2$	1.72 V	1.4 mWh/cm² at 1.7 mW/cm², rechargeable	Thin printed layers: electrodes printed on each side of a PAAM-filled paper separator + gold current collector layers evaporated on each electrode; reasonably good potential for scale-up, but production time of PAAM-filled separator needs to be reduced drastically.	Degradation of PAAM-filled cellulose separator only: complete degradation after 28 days when buried in garden soil.
10	2022	H2BQS+KOH // PBQ+OA	0.8 V	20 mWh/cm² at 0.3 mW/cm² (for 15 mL electrolyte reservoir)	Flow-cell design using 3D-printed catholyte and anolyte reservoirs; good potential for manufacturing at scale using simple 3D-printing methods, but limited to a niche application (precision agriculture).	90% biodegradation after 18 days in compost (cellulosic pads only).
11	2024	Ascorbic acid+KOH // $Fe(NO_3)_3$+OA	0.5 V	1.5 mWh/cm² at 100 µW/cm²	Semi-solid electrode design based on small molecules electrochemistry; graphene current collector layers directly generated on the cardboard substrate by laser treatment; successive hydrogel multilayer printing approach; reasonably good potential for scale-up, but laser cardboard treatment and long hydrogel solvent-casting processing times might be a challenge for high-speed roll-to-roll production.	Biodegradability not assessed; Recyclability within the paper/cardboard waste stream) assessed using the UNI 11743:2019 standard.
This work	2025	Zn / $ZnCl_2$+NH_4Cl in H_2O / MnO_2	1.05 V	6.2 mWh/cm² at 50 µW/cm²	Thin printed layers on biodegradable substrates; compatible with high speed roll-to-roll production; biodegradable packaging impervious to water-vapor ensuring a long shelf-life.	Complete degradation after 63 days when buried in compost (ASTM D5338 method).

ORR: oxygen reduction reaction; **PDMS**: polydimethylsiloxane; **PBS**: phosphate buffer solution; **PC**: propylene carbonate; **PVDF**: polyvinylidene fluoride; **PAAM**: polyacrylamide; **H2BQS**: hydroquinone sulfonic acid; **PBQ**: p-benzoquinone; **OA**: oxalic acid.

Table S1 – Summary of the most advanced biodegradable battery technologies.

Table S2 displays the requirements for each component of an all-printed biodegradable battery. Ideally, the substrate would also be the packaging material which should therefore combine the requirements of both substrate and packaging.

Component	Design requirements
All components	• Biodegradable • Non-toxic to living species and to the environment (components and degradation by-products)
Substrate	• Allows good adhesion of inks • Does not solubilize nor swell in water • Sustains the drying steps of the printing process without dimensional changes (including melting, curling or wrinkling).
Electrode binders	• Do not solubilize nor swell in water • Promote a good adhesion to the substrate/underneath layer • Compatible with the material to be printed
Electrolyte layer	• Electronically insulating • Ionically conducting • Adequate voltage stability window for aqueous electrolytes • Good mechanical strength • Printable
Packaging	• Does not solubilize nor swell in water • Impervious to water permeation • Puncture and scratch-resistant • Ideally sealable without adhesives

Table S2 – Design requirements for the components of an all-printed biodegradable battery.

SECTION 2: SUBSTRATE AND PACKAGING

2-1) Substrate development

Several biodegradable linear polyesters (all commercially available) were extruded into 100 µm thin sheets using a Davis-Standard single-screw extruder equipped with a 20 cm wide flat die then calendered between rolls. Process parameters were adjusted to achieve various surface finish (glossy or mat). One sample (PLA-PHB, commercial filament) was 3D printed to obtain a textured surface quality. All sample characteristics are displayed in **Table S3**. Two types of PLA from Total-Corbion were formulated with special crystallization agents: PLA-D (comprising Luminy D070 additive) and PLA-E (comprising ethylene bis-stearamid additive). PLA-D and PLA-E were annealed after extrusion to enhance crystallization and improve temperature resistance.

The dimensional stability of the polymer substrates was first assessed by placing them on a flat metal plate in an oven at 120 °C or 150 °C for 10 min (**Table S3**). At 120 °C, all substrates sustained 10 min with no deformation, except PBAT, which melted and re-solidified after removal from the oven. At 150 °C, PBAT and PBS showed clear evidence of deformation, but PLA and PHB substrates passed the test without deformation or curling.

Sample	Material composition	Supplier	Film production	Surface finish	Oven test		Printing test	
					120 °C [1]	150 °C [2]	Ink adhesion [3]	Drying test 120 °C [4]
PLA-D	Polylactic acid with Luminy D070 additive	Total-Corbion	Extrusion	Glossy	Pass	Pass	Pass	Pass
PLA-E	Polylactic acid with EBS additive	Total-Corbion	Extrusion	Glossy	Pass	Pass	Pass	Fail
PBS	Polybutylene succinate (PBS)	Biochem	Extrusion	Glossy	Pass	Fail	Pass	Fail
PBAT	Polybutylene adipate terephthalate (PBAT)	BASF	Extrusion	Glossy	Fail	Fail	Pass	Fail
PHB	Polyhydroxybutyrate (PHB)-based blend	Danimer	Extrusion	Mat	Pass	Pass	Pass	Fail
PLA-PHB	Blend of PLA and PHB	Mitsubishi Chemical	3D printing	Textured	Pass	Pass	Pass	Fail

[1] Oven test 120 °C: the dimensional stability is assessed after being placed on a flat surface in an oven for 10 min at 120 °C.

[2] Oven test 150 °C: the dimensional stability is assessed after being placed on a flat surface in an oven for 10 min at 150 °C.

[3] Ink adhesion: assessed by 1) flexing the printed area at a 45° angle and 2) wiping a Q-tip across the surface.

[4] Drying test 120 °C: the dimensional stability (flatness and uniformity) is assessed after printing and drying the ink at 120 °C for 10 min.

Table S3 – Thermal and printing tests on various biodegradable linear polyesters.

Screen-printing and drying trials were performed using carbon- and silver-based inks (Nagase ChemteX CI-2042 and DuPont 5025, respectively). All substrates showed a good compatibility with the ink formulations as well as good ink adhesion. However, most substrate showed signs of thermal instability during the ink drying process (10 min at 120 °C) as can be seen on **Fig. S1**. The discrepancy in results between the oven and ink-drying tests is likely caused by the ink layer shrinkage during the drying step. Only PLA-D demonstrated a satisfactory dimensional stability throughout the tests, allowing successive layers to be printed without deformation. Therefore, PLA-D and was chosen as the substrate of choice.

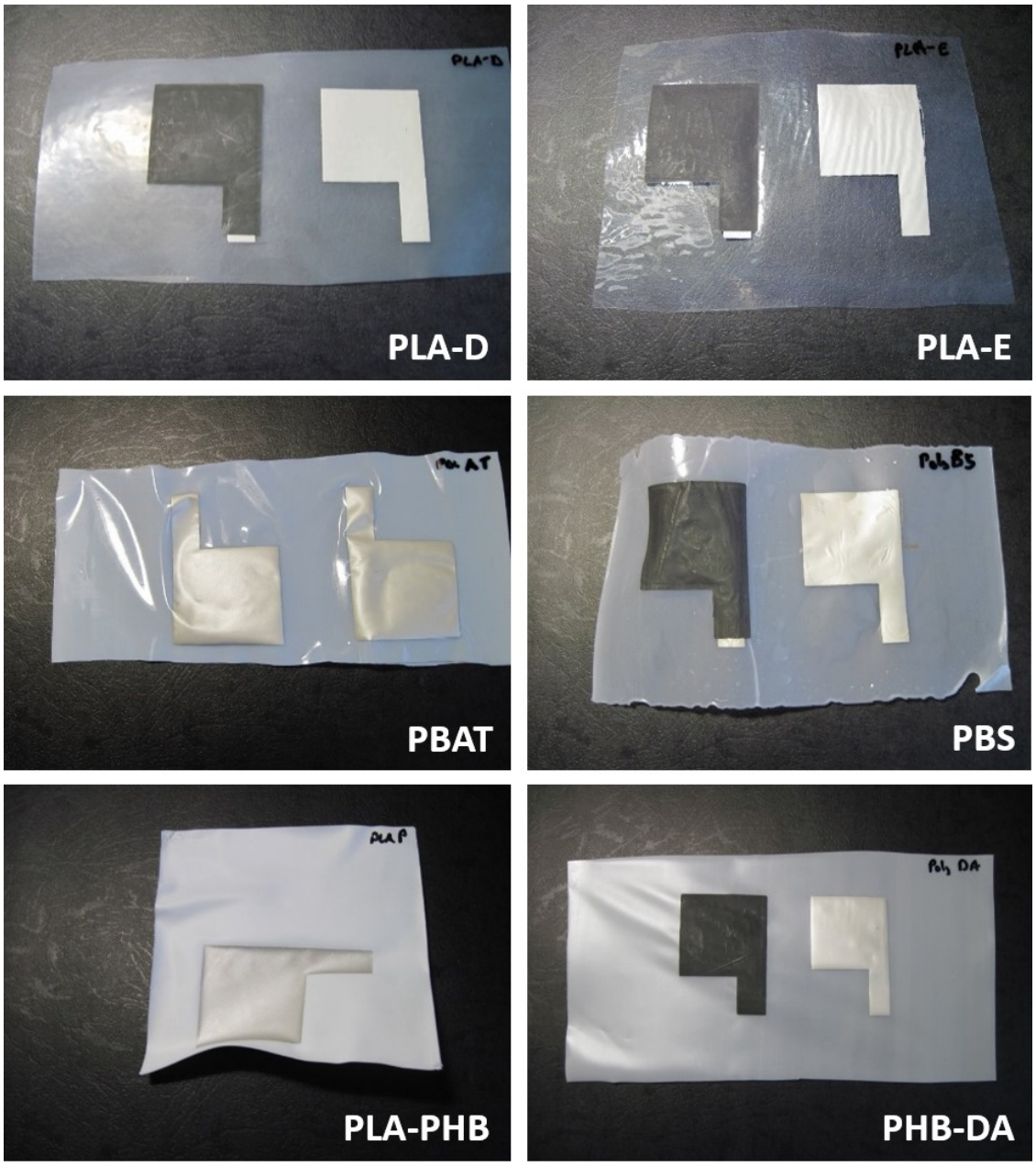

Figure S1 – Pictures showing silver and carbon-based current collector layers screen-printed on different substrates. In a few cases, the silver layers have been topped by carbon layers in a second printing pass.

2-2) Water vapor permeation testing

To test the water vapor permeation properties of the packaging materials, 5×5 cm^2 pouches were fabricated by thermally sealing 3 of the edges of two films at 170 °C for 5 s using a manual thermal sealing device, introducing a 3x3 cm^2 piece of paper fully wetted with water and thermally sealing the last edge. The water vapor permeation was monitored by regularly weighting the pouches. The PLA-D pouch dried in about 10 days, the aluminized PLA in about 14 days, and a combination of PLA-D substrate and aluminized PLA packaging was not sufficient to prevent the water evaporation (**Fig. S2**).

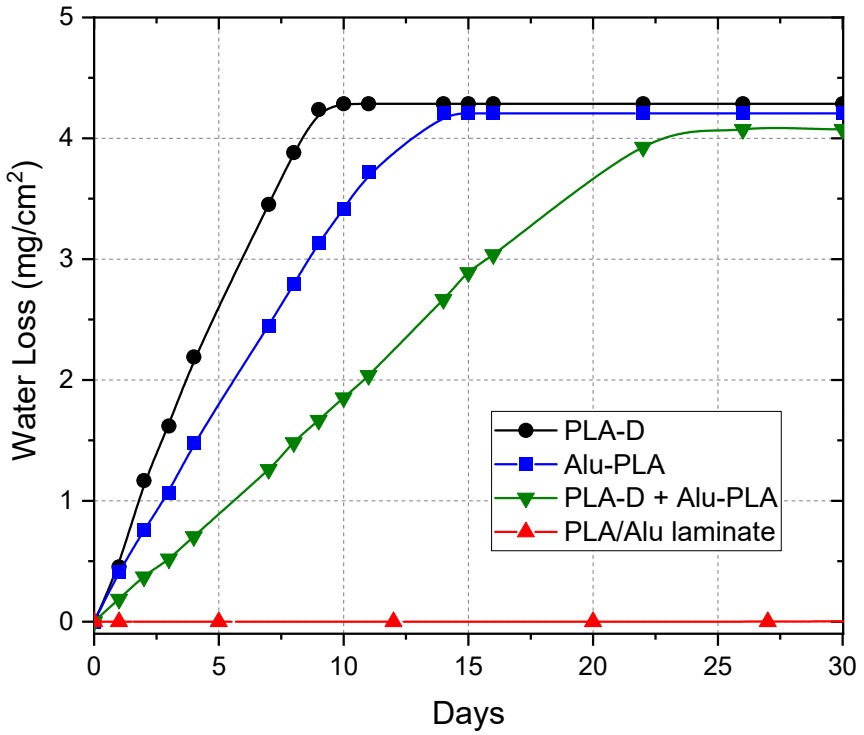

Figure S2 – Water loss by permeation through the substrate for different PLA-based films. Alu-PLA is a commercially available aluminized PLA (Celplast Enviromet [12]).

2-3) Multilayer laminate packaging development

A typical multilayer laminate is a material composed of several layers bonded together by adhesives (**Fig. S3**). The inner aluminum layer acts as a barrier to prevent both moisture and gas permeation. The key in the development of such multilayer laminates is the adhesive tie-layers.

Figure S3 – Cross-sectional drawing of the concept for a compostable multilayer laminate having an aluminum core sandwiched between two PLA films bound by a biodegradable adhesive tie-layer.

2-3-1) Compression press studies (proof of concept)

Four different types of tie-layer materials were tested to confer a good adhesion between the PLA-D film and the aluminum foil:

- A PLA-based commercial trilayer thin film supplied by Evlon (EV-HS1). One of the outer layers is treated for enhanced sealing properties, which was placed against the aluminum foil.
- A non-biodegradable polyamide-based adhesive powder from Evonik (Vestamelt Hylink)
- A polycaprolactone (PCL) from Ingevity (CAPA6500).
- An amorphous PLA grade from NatureWorks (Ingeo 8052D).

The PCL and PLA materials were obtained as pellets and were first processed into thin films, as detailed below. The PCL CAPA6500 was pressed at 100 °C under 5000 PSI for 20 min using a Carver press. The PLA Ingeo 8052D was extruded at 200 °C using a Davis-Standard single-screw extruder equipped with an 8” wide flat die kept at 200 °C. Multilayer stacks were prepared by assembling layers of aluminum (40 µm thick), tie layer and extruded PLA-D, and pressing them at a certain temperature using a Carver press. The resulting multilayer films can be considered as half the multilayer structure detailed in **Fig. S3**. However, since the aluminum layer is the one acting as a water vapour barrier layer, this half-structure is sufficient to demonstrate the barrier properties. The complete structure is only needed to protect the aluminum layer from being mechanically damaged by adding a polymer scratch-resistant layer. The complete structure can be fabricated using the same method as the half structure, using the same materials.

Specific conditions for each tie-layer are detailed below:

- Evlon: the multilayer stack was pressed at 120 °C under 5000 psi for 20 min.
- PCL: A thin film of a PCL tie-layer was obtained by pressing pellets at 100 °C under 5000 PSI for 20 min. The multilayer stack was pressed at 120 °C under 5000 PSI for 20 min.

- Amorphous PLA: The 8052D PLA is an amorphous material which exhibits tackiness at high temperatures and enables good adhesion between the semi-crystalline PLA-D and the aluminum foil. The multilayer stack was pressed at 120 °C under 5000 PSI for 20 min.
- Vestamelt: the aluminum foil was coated with a thin layer of Vestamelt Hylink adhesive powder using an electrostatic spray gun, then placed in an oven at 140 °C for 10 min. A PLA-D film was then applied to the tie-layer side of the aluminum foil and pressed at 120 °C under 5000 psi for 20 min. Although polyamide is not readily biodegradable, it is reasonable to believe that if the layer is sufficiently thin compared to the aluminum and PLA-D layers, the whole composite might be considered as compostable. In this example, the tie-layer weighted 2 mg/cm^2 whereas the half structure weighted 32.4 mg/cm^2, making the tie-layer weight ca. 6 wt% of the half structure. It can be calculated that the tie layer weight of a full symmetric multilaminate structure would be 4 mg/cm^2 out of 54.4 mg/cm^2 (7.4 wt% of non-biodegradable tie-layer).

Fig. S4 shows the water loss overtime of 5x5 cm^2 thermally sealed pouches fabricated with the four multilaminate half-structures. The first observation is that the multilayer laminates lost water at a much lower rate than the PLA-D or aluminized PLA themselves, with a rate below 0.01 mg/cm^2 per day vs. 0.5 mg/cm^2 per day for PLA-D (see **Fig. S2**). However, the tie-layers still showed varying performances. The differences are thought to arise from adhesion performance of the tie-layers. Indeed, only the internal PLA-D layer is thermally sealed and any delamination of the layers over time at the edge of the pouch will give a space for water vapour to permeate out. The best results were obtained with the Vestamelt and amorphous PLA tie-layers.

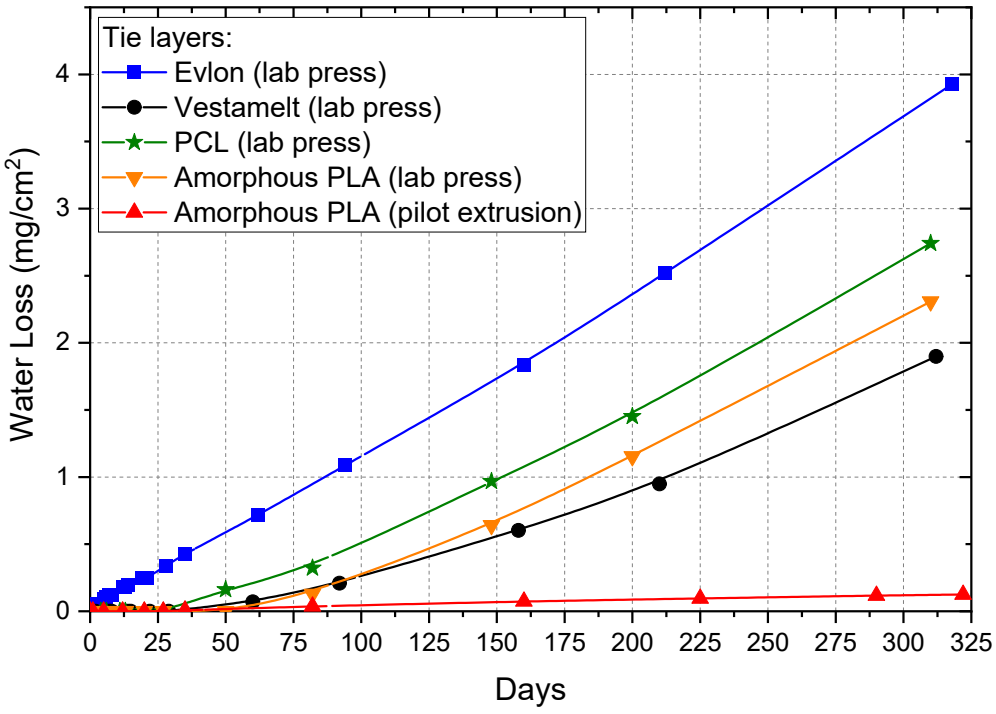

Figure S4 – Water loss over time for half-structure multi-laminates.

2-3-2) Roll-to-roll cast extrusion of half-structure multilaminate.

Since the Vestamelt is not biodegradable, it was decided to focus on the amorphous PLA for pilot-scale fabrication. Dual-layer PLA films were melt-extruded and directly co-laminated onto a 40 µm thick aluminum foil roll using a LabTech multilayer cast film line equipped with a 6" wide flat die kept at 200 °C (cf. **Fig. S5**). The top layer was the PLA-D formulation and the amorphous PLA 8052D was used as the tie-layer. The multilayer laminate was calendered between heated rolls to achieve the desired thickness. A 60 m long roll with a thickness of 150 ± 5 µm was produced.

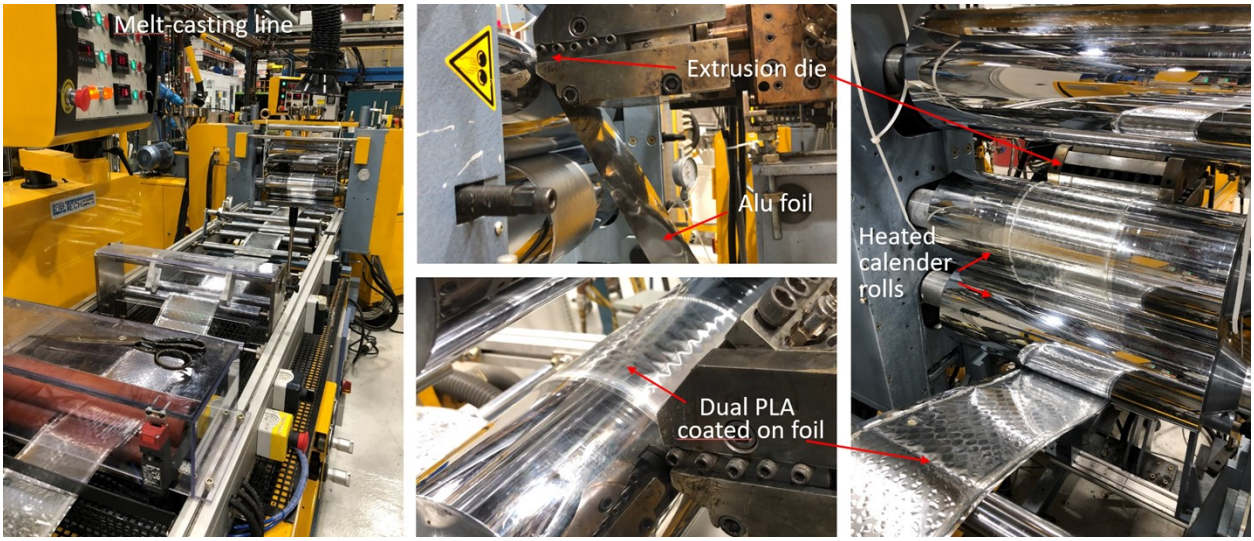

Figure S5 – Half-structure laminate pilot-scale production using a LabTech multi-layer cast film line.

Patterns can be observed on the multilayer laminate, due to a temperature discrepancy between the aluminum foil and the polymer extrudate, causing local delamination of the PLA layers from the aluminum foil. This phenomenon could be avoided by heating the roll of aluminum foil and keeping the whole extrusion head in a temperature-controlled enclosure. Such issues can be easily resolved with industrial production lines such as the ones used in the production of similar polyolefin-based multilayer packaging films for pharmaceutical or battery applications. They could not be avoided with NRC's pilot-scale equipment, however, a post thermal treatment under pressure (using a Carver press on single sheets) was efficient to eliminate the pattern and improve the adhesion. The extruded multilayer laminates demonstrated significantly lower water permeation (**Fig. S4**), indicating that the co-continuous extrusion process greatly improved the consistency of multilayer laminate production. Its rate of water loss through permeation was 4.10^{-4} mg/cm^2 per day over a period of 320 days.

SECTION 3: ELECTRODE BINDERS

A number of biodegradable polymers were investigated as binders for Zn-MnO_2 batteries. Each required specific processing conditions, some of which are detailed below. **Figure S6** presents the different biodegradable binders tested.

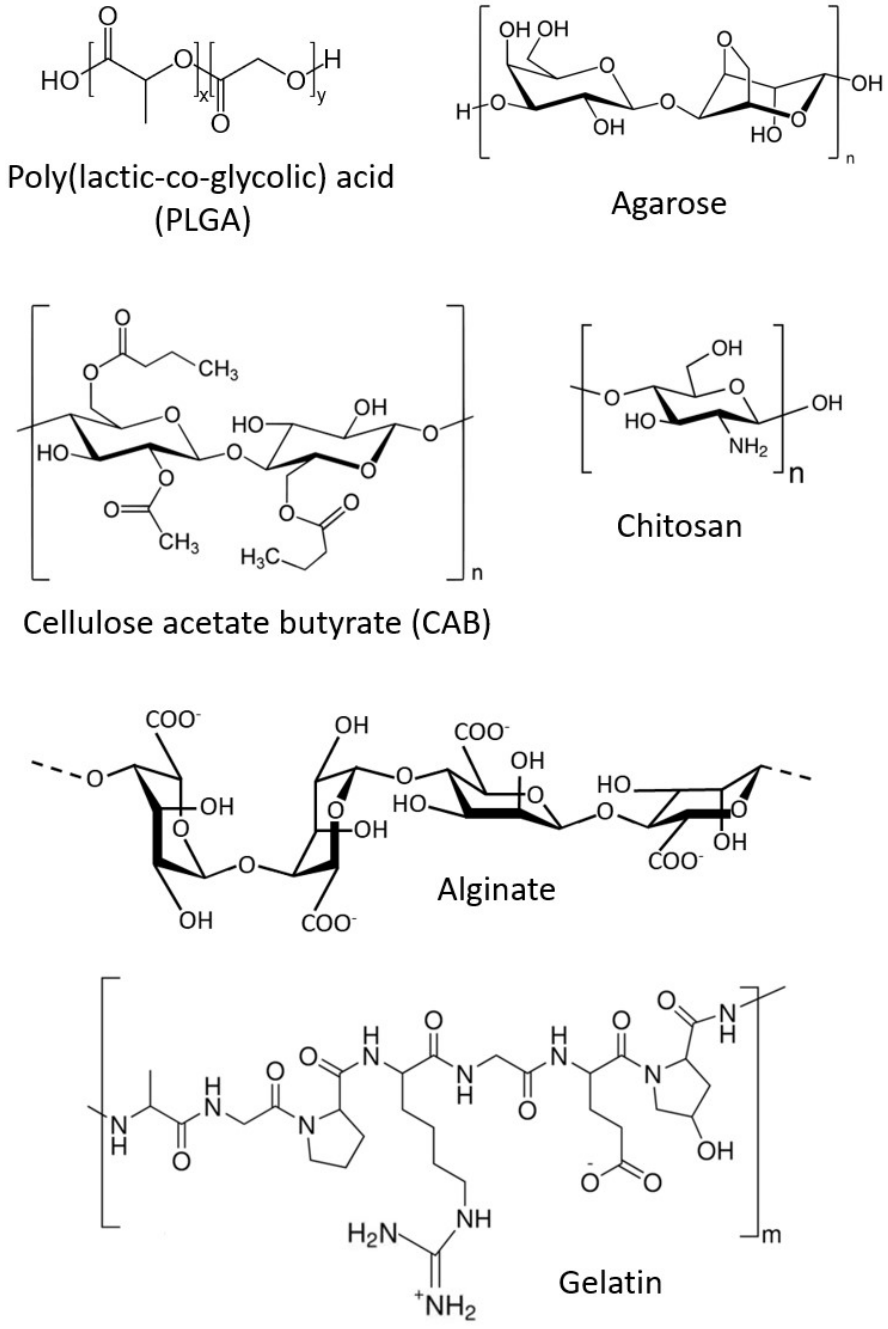

Figure S6 – Chemical structures of the biodegradable polymers investigated as electrode binders.

3-1) Preparation of chitosan-based electrodes

Chitosan, a cellulosic binder, was a potential candidate as it is only soluble in water when the pH is below its pKa (6.5). In a typical preparation of chitosan-based MnO_2 electrodes, 0.35 g of high molecular weight chitosan (Sigma Aldrich – CAS 9012-76-4) was stirred with 20 mL of 1 wt% acetic acid/deionized (DI) water until completely dissolved. The result is a clear, viscous liquid. Separately, 21.4 g of MnO_2 (> 99%, Sigma Aldrich) and 5.34 g of graphite flakes (99% carbon basis, 325 mesh, Sigma Aldrich) were ground together with a mortar and pestle until a fine powder was formed.

The solid contents were then added to the chitosan liquid mixture with stirring, and mixed until the solids were homogeneously dispersed throughout the liquid matrix (typically 0.5 hour at 400 rpm with an IKA shear mixer fitted with a 3-bladed impeller). The contents were then left to sit for 1 h prior to being cast.

The MnO_2/chitosan slurry was cast using a doctor blade onto a previously printed 10 µm thick carbon layer (commercial carbon ink Nagase ChemteX CI-2042, PET sheet substrate). The electrodes were dried at 100 ^oC for 1 h. The resulting electrode thickness was approximately 100 µm and MnO_2 loading 12.0 mg/cm^2. Final formulation of the active layer was 79 wt% MnO_2, 19.7 wt% graphite and 1.3 wt% chitosan.

3-2) Preparation of PLGA-based electrodes

Poly(lactide-*co*-glycolide) (PLGA) is a well-known polymer within the biomedical field and has already seen applications in the area of green electronics for applications such as drug delivery and biomedical implants [13-16]. PLGA can be fine-tuned to exhibit various degrees of solubility and compostability through careful selection of the molecular weight, ratio of lactide to glycolide units and terminal end-caps. Given the objective to obtain a binder-type material that is highly resistant to water solubility, a compound with a high lactide content (90%) and high molecular weight was selected. However, the 90% lactide content of the chosen polymer did pose challenges in processing. Aqueous-based solutions and light organic solvents (alcohols, glycols, acetone) were not capable of fully dissolving the polymer. Only N-methylpyrrolidone (NMP) was capable of fully dissolving PLGA. While undesirable from a “green” production perspective, the use of NMP for electrode manufacturing is standard for many Li-ion based energy storage large-scale manufacturing, and thus the infrastructure already exists to process NMP-based slurries.

In an optimal preparation of PLGA-based Zn electrodes, 10 g of Zn particles (Grillo Werke AG, 30 µm alloyed particles, 300 ppm Bi, 300 ppm In) was added to 2 mL of PLGA pre-dissolved in NMP (17.6 wt%). The slurry was mixed at 2000 rpm for 15 min in a MAZERUSTAR planetary mixer to yield a homogeneous slurry. Electrodes were coated onto carbon or silver current collector layers pre-printed on PET sheets at a thickness of ca. 100 µm. The electrodes were first dried at 80 °C in air to remove a majority of the NMP, followed by vacuum drying at 95 °C for a minimum of 30 min prior to use. Final formulation of the active layer was 96.5 wt% Zn, and 3.5 wt% PLGA. Lower PLGA contents led to electrode cracking and delamination from the current collector. PLGA-based MnO_2 electrodes were produced following a similar procedure, with a final active layer composition of 74.8 wt% MnO_2, 16.4 wt% graphite and 8.8 wt% PLGA.

3-3) Preparation of CAB-based electrodes

Cellulose acetate butyrate (CAB) is a cellulose-based polysaccharide bearing acetate and butyrate functionalities, widely used as a binder for coatings [17]. It is insoluble in water, due to the replacement of most of its hydroxyl functional groups by acetate or butyrate functions (cf. **Fig. S4**), which makes it a good binder candidate for aqueous electrolytes. Being soluble in NMP, the procedure first developed with PLGA was used to assess CAB's suitability as electrode binder. Optimal electrode formulations were the same as for PLGA binder. The use of CAB binder provided strongly adhesive layers for both Zn and MnO_2, with excellent structural properties.

3-4) Preparation of alginate-based electrodes

Sodium alginate (SA) is a cellulose-based polysaccharide soluble in water. Its unique structure is composed of *α-L-guluronic acid* and *β-D-mannuronic acid* blocks (G and M blocks). Interestingly, the G blocks can be crosslinked using divalent cations, such as Ca^{2+}, rendering it insoluble [18,19]. This is particularly suitable for Zn aqueous batteries whose electrolytes always contain Zn^{2+} cations, which can potentially serve as crosslinkers.

In a typical preparation of alginate-based electrodes, 1 g of sodium alginate (from brown algae, Aldrich) was first dissolved in 18 mL of DI water with the help of heating and stirring until complete dissolution, then cooled down to room temperature. For the Zn slurry, 98 g of Zn particles (GN 3-0 grade, alloyed with 300 ppm In and 300 ppm Bi, 30 µm, Grillo Werke AG) and 16.5 mL of alginate solution were added to 2.5 mL of glycerol and 100 g of 1/8" diameter stainless-steel shots in an attritor, and the slurry was mixed overnight, then collected through a sieve to remove the stainless-steel shots. For the MnO_2 slurry, the Zn was replaced by a mix of 21.38 g MnO_2 (reagent grade, Aldrich) and 5.35 g of graphite (Imerys KS6), to which, 9 mL of water and 5 mL of alginate solution were added. The slurry was mixed overnight in the attritor before being collected through a sieve. Slurries were coated onto carbon current collector layers pre-printed on PET sheets at a thickness of ca. 100 µm. The electrodes were dried at 80 ^{o}C in air for 1 h. Alginate content in the electrodes was typically between 0.93 and 1 wt%.

The electrodes were then dipped into either the battery electrolyte (containing $ZnCl_2$ and NH_4Cl salts) or pure water, expecting that the Zn^{2+} ions would serve as crosslinkers**. Figure S7** shows that both Zn and MnO_2-based active layers did not dissolve when exposed to the battery electrolyte whereas it gradually dissolved when exposed to pure water (**Fig. S7 a,b and d,e**). This demonstrated the effective crosslinking of the alginate binder by the divalent Zn^{2+} cations. In another control experiment (**Fig. S7 c,f**), Zn and MnO_2 electrodes were first soaked for 5 min in the battery electrolyte, and then dipped into pure water. It showed an excellent stability, suggesting that Zn^{2+} ions have been trapped into the alginate structure, maintaining its physical stability afterwards.

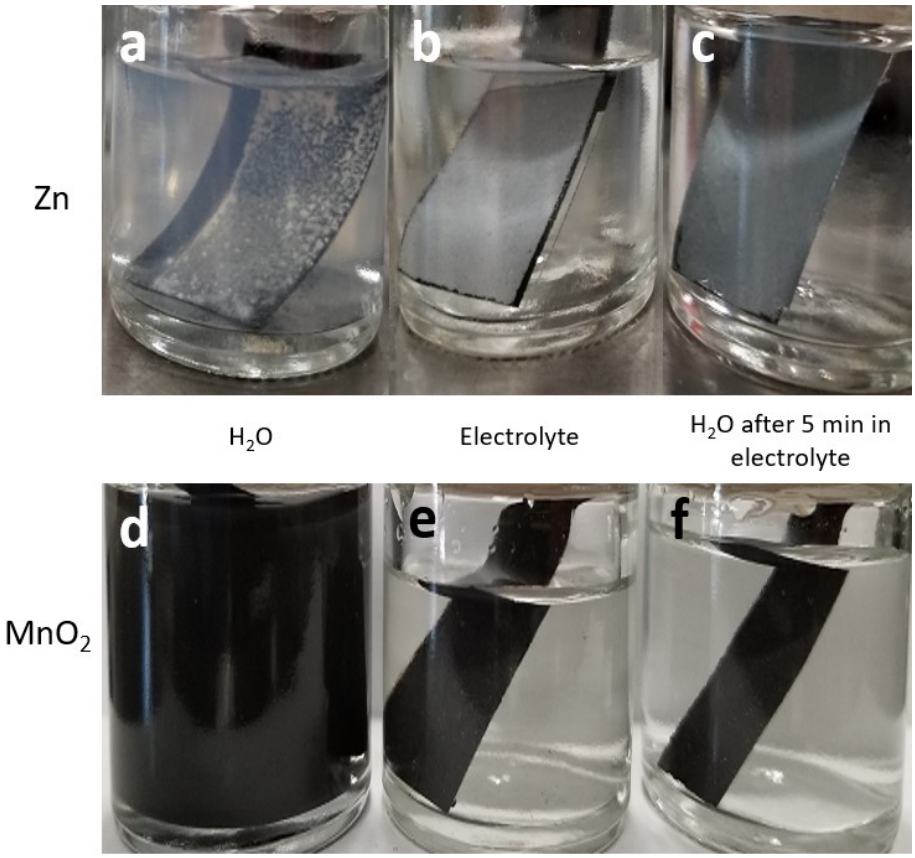

Figure S7 – Zn (a-c) and MnO_2 (d-f) active layers with 1.1 wt% alginate binder after 1 week immersion in deionized water (a, d), $ZnCl_2$-NH_4Cl electrolyte (b, e), or deionized water after soaking for 5 min in $ZnCl_2$-NH_4Cl electrolyte (c, f).

Binders were rejected for various reasons:

1. Some of the binders were found to lead to chelation when mixed with Zn, such as agarose and chitosan, which prevented their use for the Zn active layer (**Fig. S8a**).
2. A further drawback of chitosan, when used for MnO_2 electrodes was the acidity of the inks (see preparation details below), which caused a significant deterioration of the screens employed in the screen-printing process.
3. Gelatin formed a slurry that could be cast, resulting in well-dispersed Zn or MnO_2 films that strongly adhered to the glass surface (**Fig. S8b**). However, gelatin-bound electrodes did not withstand exposure to the aqueous electrolyte, resulting in significant swelling and loss of mechanical stability. Agar-based MnO_2 electrodes were also unstable with time when exposed to the battery electrolyte (swelling and delamination from the substrate were observed).
4. PLGA-based MnO_2 electrodes were not stable over time, which was found to be related to a structural degradation of the carbon current collector underneath.
5. CAB's hydrophobic properties led to poor electrochemical performances.

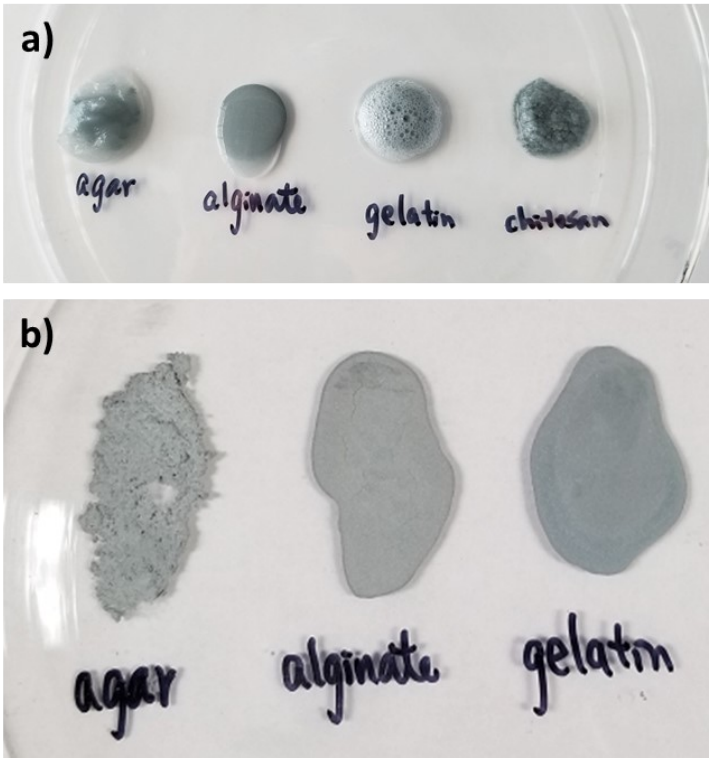

Figure S8 – a) Aqueous slurries of zinc of some of the biodegradable binders, with observable chelation for chitosan and agarose; b) coating tests onto glass surface for some of the biodegradable binders.

3-5) Investigations of biodegradable binders for carbon current collectors

Chitosan was the first biodegradable binder investigated for printed current collectors. To produce the carbon/chitosan current collectors, first a series of slurries were produced to optimize conductivity while also still being screen printable. To do this, a constant mass ratio of 2.4:1 of graphite:carbon black (Imerys Timrex KS6 and Imerys C45, respectively) was utilized based on preliminary experiments, to achieve the highest conductivity, also in agreement with literature results [20]. The carbon materials were mixed with various amounts of liquid comprised of 1 wt% acetic acid/chitosan and stainless-steel shots in an attritor at 40 rpm for 1 h. As a standard, the chitosan content was kept at 0.4 g chitosan per 25 mL of liquid. The resulting smooth, homogeneously dispersed ink was then screen-printed at various thicknesses, and dried at 100 ^{o}C for 30 min. The surface of the electrode was wiped to remove any free carbon black particles and to expose a smooth surface for conductivity measurements.

The critical parameter for increasing conductivity was clearly the ratio of carbon:liquid, as evidenced in **Fig. S9a**. The conductivity of various casted slurries was measured using a two-point probe 1 cm apart. Based on this information, a maximum conductivity was achieved with carbon:liquid mass ratio of 0.2. At ratios of 0.24, the conductivity decreased, likely due to the high carbon loading of said slurry creating screen-printing difficulties, and general poor integrity of the printed electrode. An image of the

produced electrodes under optimal conductivity formulations are shown in **Fig. S9b.** The electrodes were quite flexible with no delamination from the PET substrate.

To properly compare the conductivity of the produced current collectors to that of commercially available inks, 4-point probe conductivity tests were performed on 5 different electrodes of the optimized slurry, as determined previously. The summarized results, shown in **Fig. S9c,** demonstrate the as-produced chitosan-based carbon current collectors have a resistivity approximately 2 times greater than that of the commercial Nagase ChemteX CI-2042 and Loctite commercially available inks.

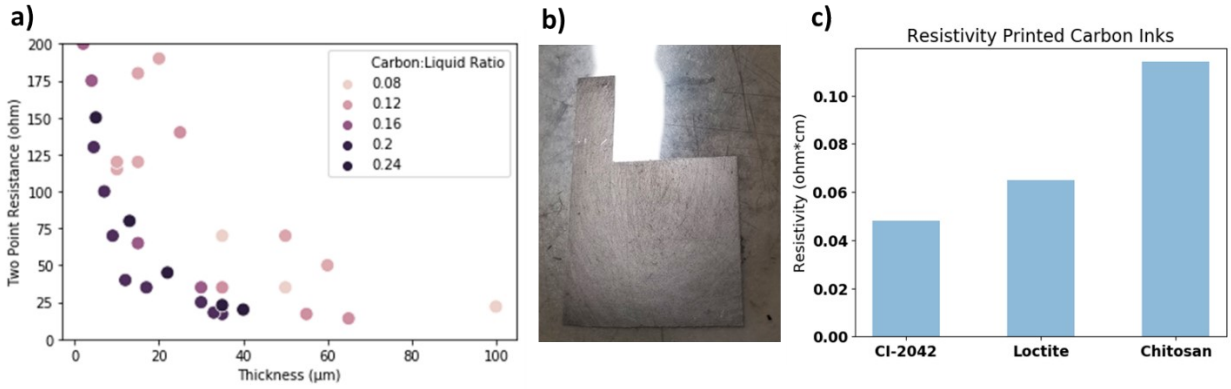

Figure S9 – a) 2-point resistance (1 cm) of various carbon:liquid ratios, coated at different thicknesses; b) image of a chitosan-based current collector layer with optimized 0.2 carbon:liquid ratio; c) 4-point probe resistivity of carbon-based (commercial) and chitosan-based current collector layers.

Attempts to use PLGA as a carbon current collector binder was not successful. Most of the carbon particles were found to separate from the polymer matrix upon drying, settling as a fine dust on top of it. Close examination showed that the actual carbon concentration within the binder was quite low (**Fig. S10a**). On the other hand, when CAB was used as the binder for the carbon current collector, mechanically robust films were obtained with no separation of the carbon from the polymer matrix. An optimized CAB current collector slurry was comprised of 15 mL stock solution (0.32 g CAB/3 g NMP), mixed with 1.5 g KS6 graphite and 0.6 g C45 carbon black. The contents were mixed for 20 min at 400 rpm using a shear mixer. Electrodes were produced by casting the carbon film at ~35 µm, resulting in a robust film with a majority of the carbon suspended evenly throughout the polymer matrix (**Fig. S10b**). Typical resistances for 35 µm thick films were 150 Ω (measured at 1 cm probe distance, as in **Fig. S9a**), which is significantly higher than commercial carbon inks or the previously developed chitosan carbon inks. Moreover, attempts to coat CAB-based Zn electrodes onto CAB-based current collector were not successful. The adhesion of the first layer of Zn particles was strong, but the particle-to-particle adhesion of the rest of the Zn material was very poor, as shown in **Fig. S10c**. The postulated reason is the use of the same binder/solvent system for both layers, resulting in the CAB binder being partially absorbed into the carbon sublayer, depriving the top Zn particles from its binding properties. Resulting films showed extremely weak Zn-Zn particles adhesion, causing a majority of the electrode to crumble. The same phenomenon was not observed with CI-2042 carbon sublayers. As a control experiment, Zn-CAB slurries

were coated onto thinner carbon-CAB current collector layers (10 µm), in order to limit the binder absorption by the carbon sublayer. In this case, the resulting Zn film was more robust, and behaved very similar to the strong Zn-CAB film cast onto a CI-2042 layer. However, the low conductivity of such a thin carbon layer (values of 750-1000 Ω/cm at 10 µm, nearly 10× higher than that of CI-2042) resulted in poor electrochemical performance, with an overpotential > 0.5 V upon discharge, preventing the cell operation.

Attempts were made to coat a CAB/Zn slurry on top of the chitosan-based carbon current collectors previously developed. However, the incompatibility of the chitosan and the NMP solvent caused a very poor wettability of the Zn slurry on the carbon layer, resulting in an extremely poor adhesion of the Zn layer on top of the carbon layer (**Fig. S10d**).

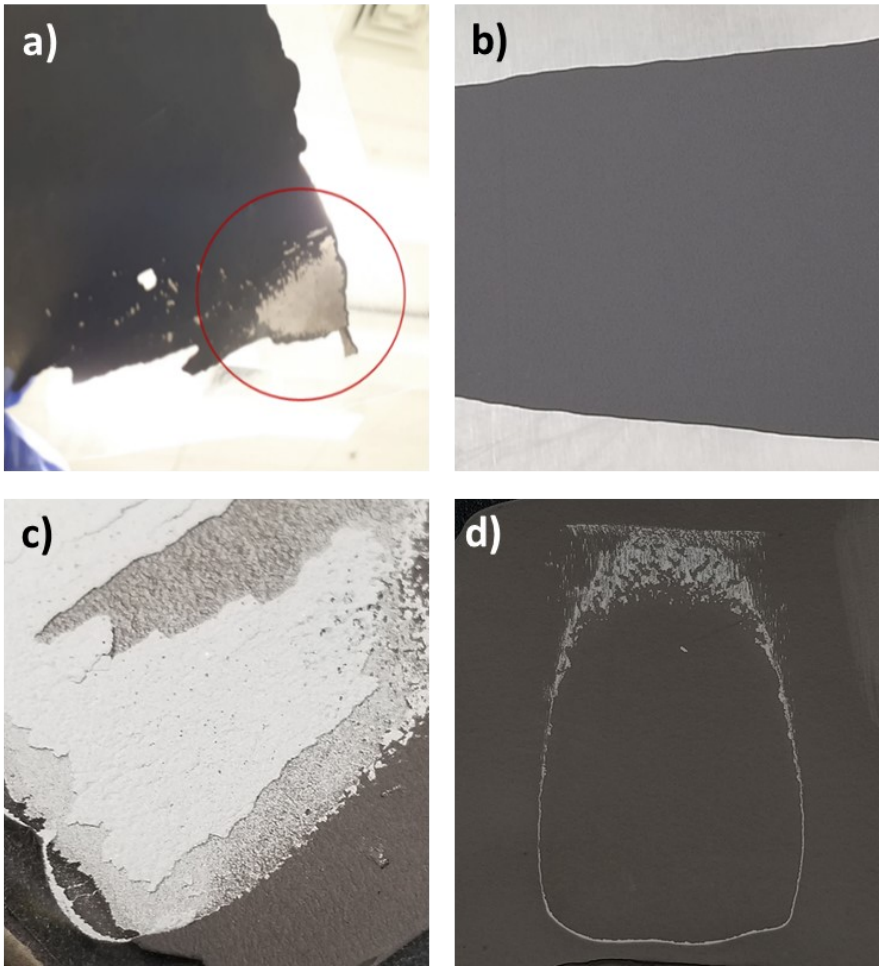

Figure S10 – a) Carbon-PLGA with the carbon surface dust mechanically removed (red circle). The remaining polymer layer is almost clear, showing that most of the carbon particles have phase-separated out of the layer during drying; b) Casted carbon electrode with CAB as the carbon binder; c) Zn-CAB layer coated on top of a CAB-carbon current collector; d) Remains of Zn-CAB layer coated onto a carbon-chitosan layer.

SECTION 4: GEL POLYMER ELECTROLYTE DEVELOPMENT

Summary of GPE development

The idea was to develop a biodegradable gel polymer electrolyte (GPE) that could be formulated as a printable ink and then solidified using an ultrafast crosslinking process using ultra-violet (UV) radiation. It was developed in three stages, as detailed below.

During the first stage (GPE#1), the concept of formulating a printable precursor electrolyte solution followed by rapid UV curing (< 5 min) was demonstrated (**Section 4-1**). One noteworthy development was the demonstration of UV curing in ambient air. Oxygen deactivation of radical initiators is a common issue, which adds cost and complexity to the manufacturing infrastructure [21,22]. The use of phenyl bis(2,4,6-trimethylbenzoyl) phosphine oxide (BAPO) as a photo-initiator led to a formulation resistant to oxygen inhibition during curing [23-25]. At this stage, the mechanical requirements for a suitable GPE system for battery application were also investigated. It was established that a Young's modulus of 0.1 MPa was the minimal mechanical strength required to avoid short-circuiting the cell by applying pressure. The optimized GPE#1 had a typical Young's modulus of 0.17 MPa (**Fig. S12**). Its ionic conductivity reached 130 mS/cm at room temperature in a 2M NH_4Cl electrolyte at room temperature (**Fig. S13**), which is equivalent to a liquid 2M NH_4Cl electrolyte without polymer gel [26].

After the successful demonstration of rapid UV-curing of a GPE precursor solution, the development of a biodegradable version was undertaken. Ideas were based on hydrogels typically used for biomedical applications [27-30]. A PCL-PEG-PCL triblock copolymer acrylated on both ends (GPE#2) was designed as a macromonomer that could be UV cured to produce a robust hydrogel (**Section 4-2**). The PCL sections provided the biodegradable functionality along the polymer chain. At this stage, the UV crosslinking time was reduced to 1 s by using lithium phenyl-2,4,6-trimethylbenzoylphosphinate (LAP) (a water-soluble photo-initiator) and powerful UV lamps (Phoseon FJ200 12W FireJet). LAP was also found to be insensitive to oxygen deactivation. The toughness of GPE#2 was found to be higher than GPE#1 (typically ~0.46 MPa, independent of salt molarity (**Fig. S18**). At this stage, long term stability issues of the electrolyte were investigated in electrochemical cells, which led to an optimized salt formulation of 2.9M $ZnCl_2$ and 0.9M NH_4Cl (see **Figs. S19-22** and related discussion). The room temperature conductivity of GPE#2 with the optimized salt formulation was 70 ± 15 mS/cm, which is slightly lower than GPE#1 but largely sufficient for battery operation.

However, being mostly made of PEG, GPE#2 was still considered unsatisfactory in terms of biodegradability. Indeed, although certain microorganisms have been found to biodegrade PEG, they are relatively rare and therefore do not confer a broad biodegradability for GPE#2 [31]. The design of a fully biodegradable GPE system was therefore undertaken, which led to the successful development of an acrylated PVA-*g*-PCL graft copolymer, both moieties being well known biodegradable polymers [32] (**Section 4-3**). However, the system was significantly more complex than the GPE#2 triblock copolymer system, since the PCL growth can be initiated on any hydroxyl group of the PVA main chain, which means that multiple versions of the graft copolymer can be obtained depending on the synthesis

parameters, resulting in a variety of materials. Multiple iterations of development were necessary to produce a copolymer having the adequate combination of properties. Finally, synthetic path simplification, various optimizations and synthesis scale-up were undertaken, allowing to obtain 400-500 g batches with high quality and reproducibility.

The following sections describe the successive developments of the biodegradable and printable GPE layer.

4-1) Development of GPE#1 (PAA+PEO)

The first proof of concept was developed by adapting a concept proposed by Braam et al. [33]. Their idea was to prepare an aqueous solution with acrylic acid, a crosslinker (polyethylene glycol divinyl ether), a photo-initiator (Irgacure 2959), as well as a pH regulator (potassium hydroxide) and a viscosity enhancer (polyethylene oxide), then cast the aqueous formulation onto a substrate to form a film and polymerize/crosslink it under UV light for 10 min, which yielded a solid, yet flexible hydrogel. Although efficient, the method still had a critical disadvantage: it required the further impregnation of the hydrogel with an electrolyte (KOH solution in this case), which is not convenient for industrial production. Moreover, the UV radiation could only be performed under anaerobic conditions (since oxygen deactivated the photo-initiator), which would add complexity and cost to an industrial production operation.

This concept was adapted and improved by replacing the polyethylene glycol divinyl ether with tetraethylene glycol divinyl ether (TEGDVE), to strengthen the hydrogel by shortening the crosslinking segments, and by replacing the Irgacure 2959 photo-initiator with a phosphine-based one, phenylbis(2,4,6-trimethylbenzoyl) phosphine oxide (BAPO), which proved to be much more immune to oxygen deactivation, thanks to its longer wavelength absorption of UV light allowing a deeper penetration into the film, resulting in a more in-depth cure. **Figure S11a** shows the polyacrylic acid (PAA) synthesis mechanism via UV-initiated radical polymerization. GPE#1 also contained polyethylene oxide as a viscosity enhancer.

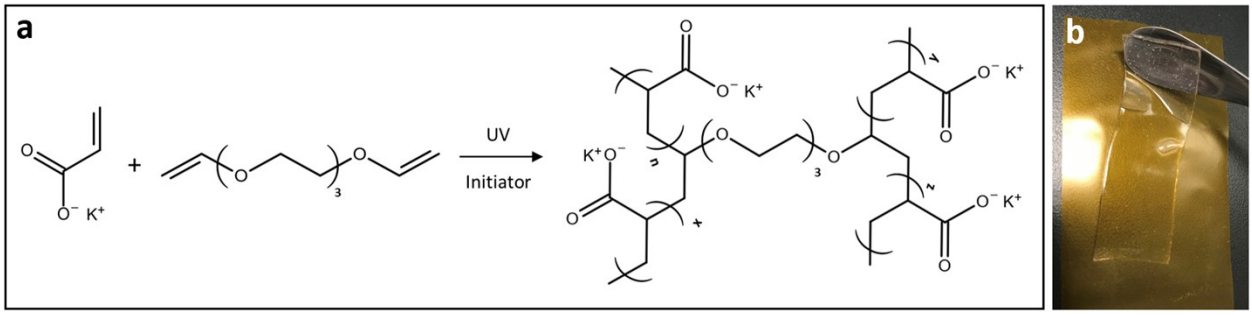

Figure S11 – a) Mechanism of acrylic acid UV-initiated radical polymerization and crosslinking using TEGDVE (adapted from Braam et. al [33]; b) Photograph of a GPE#1 film obtained by solvent casting and UV-curing for 5 min.

The formulation's optimization was carried out using a design-of-experiment (DOE) approach, which allowed to identify the acrylic acid concentration and UV curing time as the 2 parameters having the most influence on the overall properties of the GPE (detailed study not shown). The optimal GPE#1 formulation was: 15 wt% of acrylic acid, 12 wt% of potassium hydroxide, 24 wt% of polyethylene oxide (600.000 g/mol, from Polyscience), 1.5 wt% TEGDVE, 5.0 wt% BAPO, 6.5 wt% NH_4Cl (2M) and 36 wt% H_2O. GPE films were typically obtained by weighting and mixing the components of the precursor solution in a vial, casting the solution on a glass plate, placing a second glass plate above, with shims of specific thickness, then curing the film for 5 min using a Dymax BlueWave 200. An image of the resulting GPE#1 film is shown on **Fig. S11b**.

The mechanical properties of the GPE#1 were characterized using an Instron 5548 MicroTester (see **Fig. S12**) using a 5 kN load cell. Special fixtures were designed and fabricated to enable the characterization of small size polymer samples in compression mode. Samples were cut into disks 10 mm in diameter and placed on the lower part of the fixture. The pressure sensor was then lowered on top of it. The Young's modulus was determined by measuring the force applied to the sample during a progressive compression experiment at 1 mm/min in a controlled atmosphere (22 °C, 50 % RH).

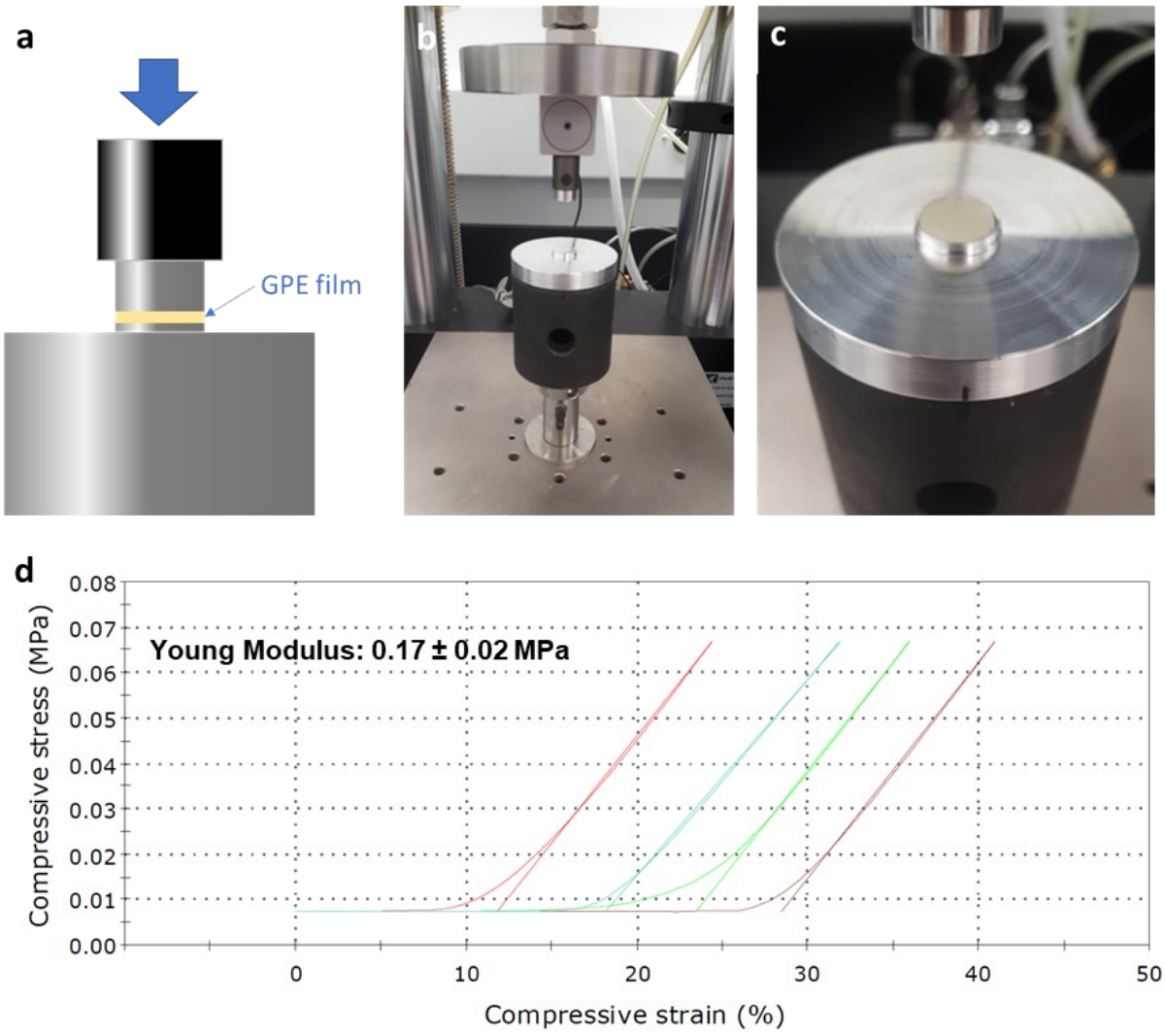

Figure S12 – a) Scheme showing the compression test methodology. B) and c) photographs of home-made test fixtures; d) Strain-stress curves obtained with the optimized GPE#1 formulation.

The ionic conduction properties of the GPE#1 were tested by placing a 13 mm diameter disc between 2 stainless steel electrodes connected to a VMP3 multipotentiostat (Biologic, France). The ionic resistance was measured using electrochemical impedance spectroscopy (EIS) at room temperature. **Figure S13** shows the results of ionic conductivity vs. salt content for GPE#1.

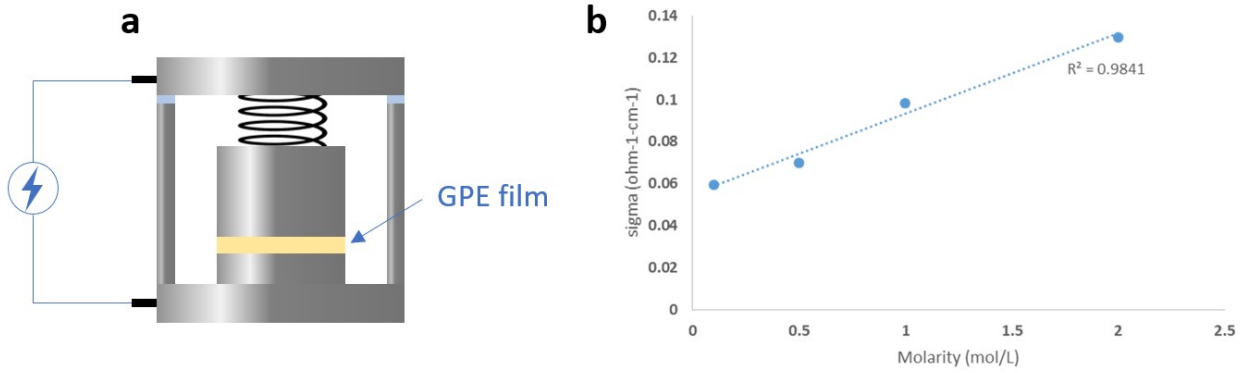

Figure S13 – a) Scheme of the conductivity testing setup using an ECC-Std cell (EL-CELL, Germany) whose base was modified for conductivity measurements; b) ionic conductivity of GPE#1 films cast with different salt concentrations (derived from EIS measurements).

4-2) Development of GPE#2 (based on acrylated PCL-*b*-PEG-*b*-PCL)

The concept for GPE#2 was derived from UV-crosslinked hydrogels prepared for biomedical applications[16-18]. Such hydrogels, based on block-copolymers bearing acrylated functional groups, are relatively simple to synthesize and have been shown to provide strong mechanical properties while remaining flexible and able to incorporate significant amounts of water. Moreover, the presence of PCL blocks provides the opportunity to biodegrade the main chain. The synthesis was adapted from previous reports, as detailed below.

4-2-1) Synthesis of PCL-b-PEG-b-PCL-diacrylate

Figure S14 shows the 2-step reaction for the synthesis of the acrylated triblock copolymer. The hydroxyl end functions of PEG were used to initiate the ε-caprolactone polymerization. Acrylation of the terminal hydroxyl groups was performed in a second step. Optimization studies were carried out to efficiently remove the triethylammonium chloride byproduct salt (a contaminant that led to product degradation and auto-polymerization during storage) and recrystallize the diacrylate macromonomer product.

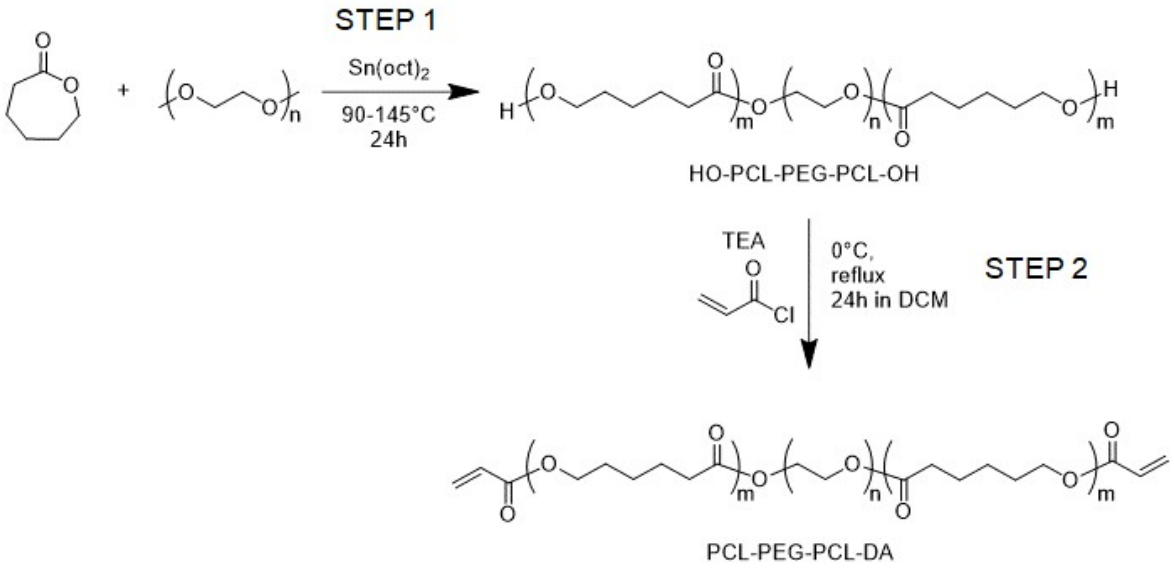

Figure S14 – Mechanism of the 2-step reaction for the preparation of the diacrylated macromonomer.

An optimized typical synthesis was carried out as follows:

Step 1:

To a 250 mL 1-necked round-bottomed flask was added a football-shaped stir bar, followed by 21.24 g PEG (Mw 20K, 1.06 mmol). A vacuum line was attached, and the flask was heated to 170 °C with stirring for 30 min to remove water. The solid PEG melted and became a viscous syrup consistency. The flask was then cooled to 90 °C and purged with N_2. Next, 4.85 g (42.5 mmol) of distilled ε-caprolactone and 1 drop of tin (2-ethylhexanoate) (approx. 30 mg) were added. A Dean-Stark trap and condenser were attached to the flask and capped with a needle for N_2 purging. The reaction was allowed to stir at 150 °C overnight. The flask was cooled to room temperature, and the crude polymer melt solidified to form a hard, waxy, whitish solid. The solid polymer product was dissolved in 100 mL of dichloromethane with stirring to yield a peach-colored solution. This dichloromethane solution was slowly poured into two separate 1 L beakers each containing 600 mL of vigorously stirred diethyl ether to precipitate the triblock PCL-PEG-PCL polymer as a fine white powder. The precipitated polymer was filtered on a coarse porosity sintered frit, washed 1× with 50 mL diethyl ether, and dried in a recrystallization dish overnight at 35 °C. 21.4 g of polymer recovered as a white powder (82 % mass recovery).

Step 2:

To a 1 L 3-necked round-bottom flask was added a large stir bar, followed by 700 mL THF. With vigorous stirring, 43.5 g of PCL-PEG-PCL diol (from step 1, Mw~20,600 by ^{1}H NMR) was gradually added. An N_2 purge line was attached to the reaction, and 0.88 mL of triethylamine (0.64 g, 6.3 mmol, 3 equivalents) was added. Next, 0.51 mL of acryloyl chloride (6.33 mmol, 3 equivalents) was slowly added dropwise, and a reflux condenser was attached to the flask. The reaction was heated to 80 °C and allowed to stir overnight in the dark. After overnight stirring, the reaction was allowed to cool back down to room temperature. The reaction solution was a hazy suspension. After cooling, the mixture was filtered through a Whatman#4 filter paper to remove the triethylammonium chloride salt, and the filtrate was concentrated using a rotary evaporator, furnishing the crude diacrylate product as a waxy, sticky solid.

This solid was isolated, and gradually added to a 1 L beaker of rapidly stirred 2-propanol. The suspension was allowed to mix overnight in the dark. After overnight stirring, the triturated solid suspension was filtered through Whatman #4 filter paper and the solid residue was re-suspended in 1 L of diethyl ether, stirred for 30 min, and filtered. The final product was air-dried in a recrystallization dish to furnish 38.4 g of dried product (88 % mass recovery). The macromonomer was stored at 4 °C in a refrigerator.

Figure S15 presents a ^{1}H NMR characterization of an optimized triblock copolymer diol (intermediate product). Peak integration was used to determine the PCL block size, which was typically around 500 g/mol. **Figure S16** shows the ^{1}H NMR of the diacrylated macromonomer. The final product contained less than 10 ppm triethylammonium chloride salt.

Figure S15 – ^{1}H NMR characterization of the triblock copolymer diol.

Figure S16 – ^{1}H NMR characterization of the triblock copolymer diacrylate.

The GPE#2 precursor solution was prepared by dissolving the diacrylate triblock copolymer in water, together with NH_4Cl and a UV photo-initiator. Lithium phenyl-2,4,6-trimethylbenzoylphosphinate (LAP) was used as a replacement for BAPO to take advantage of its better water solubility and efficiency at low loadings. GPE#2 precursor solutions were prepared by simply dissolving diacrylate triblock copolymer together with LAP in the pre-mixed electrolyte solution. The rheology was optimized for optimal screen-printing. Optimized formulation was 35 wt% of diacrylate triblock copolymer and 0.2 wt% of LAP photoinitiator. The resulting solution is shown in **Figure S17**, together with a resulting GPE#2 screen-printed on a PET thin sheet.

GPE#2 was found to be much stronger than GPE#1, with Young's modulus values around 0.46 MPa (**Fig. S18a**) while still maintaining a very good flexibility. The Young's modulus was found to be relatively independent of salt molarity (**Fig. S18b**).

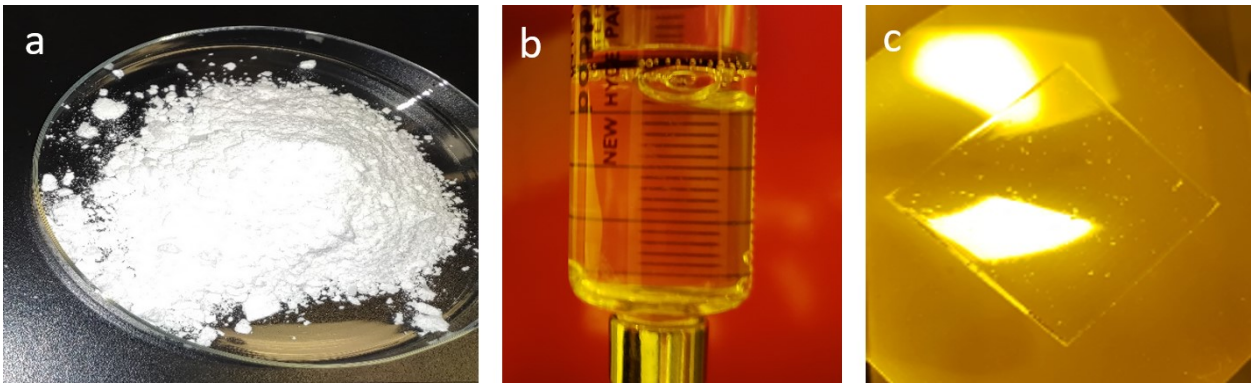

Figure S17 – a) Triblock copolymer diacrylate; b) GPE#2 precursor solution in water; c) screen-printed and UV-cured GPE#2 polymer electrolyte.

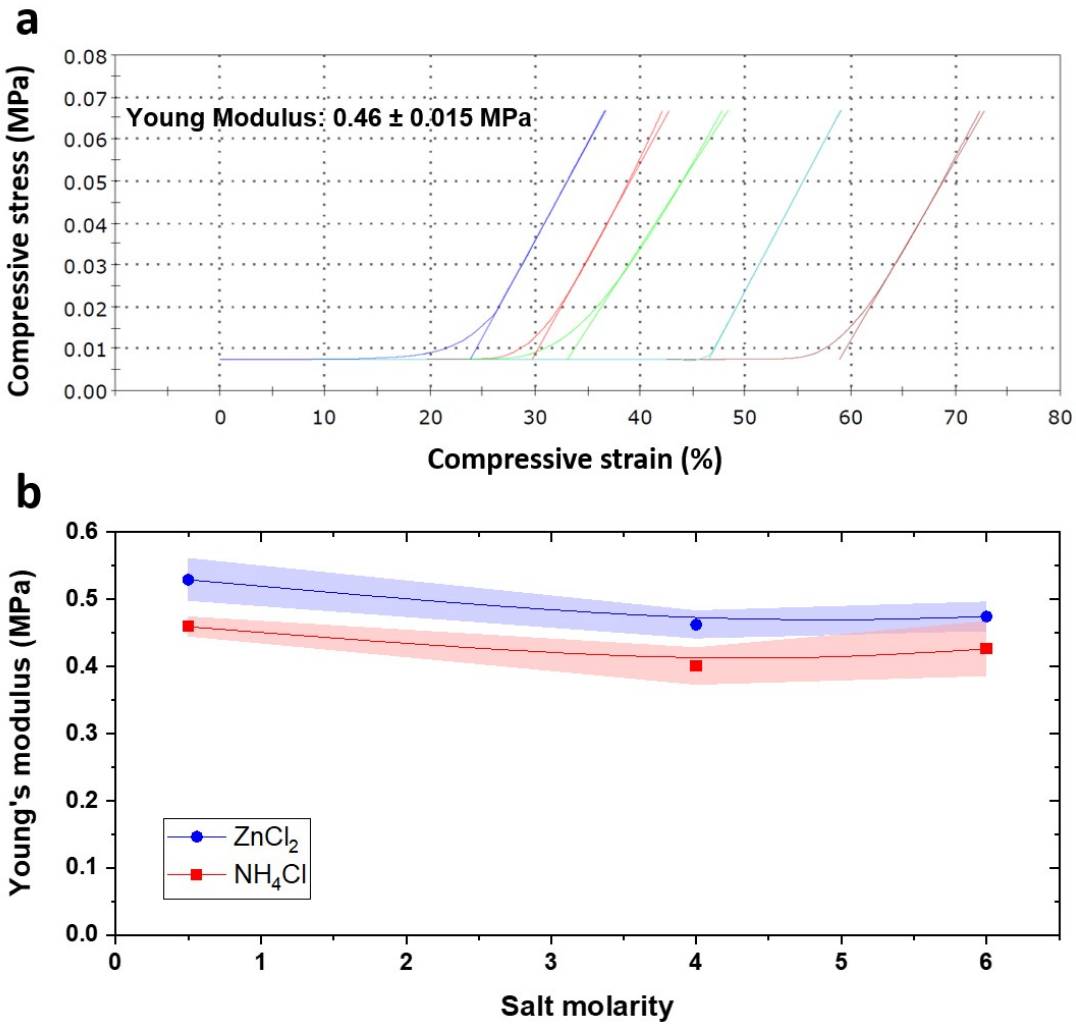

Figure S18 – a) Typical strain-stress curves obtained with a GPE#2 formulation (here 0.5 M NH_4Cl); b) Young's modulus of GPE#2 formulations with various salts and molarity (calculated from strain-stress curves).

Investigation of stability issues:

Long-term stability issues were observed with GPE#2 thin films, involving corrosion of Zn electrodes and salt precipitation inside the gel over time. After a short period of open circuit voltage (OCV) for cells comprised of 4M or greater NH_4Cl (typically between 5-50 hours), the voltage decayed rapidly to ~1 V and became erratic (see **Fig. S19a**). At 0.5 M NH_4Cl, this precipitate was not an issue, but the cell voltage was initially lower (below 1.25 V) due to the low salt concentration. This voltage decay corresponded to the formation of a white precipitate at the Zn/electrolyte interface (**Fig. S19b**). The corresponding powder X-Ray diffraction pattern identified the precipitate as zinc diamine chloride ($Zn(NH_3)_2Cl_2$) (**Fig. 20**). Measurement of the electrolyte pH was precipitate was 7.5, roughly 2 orders greater than the electrolyte starting pH of 5.5.

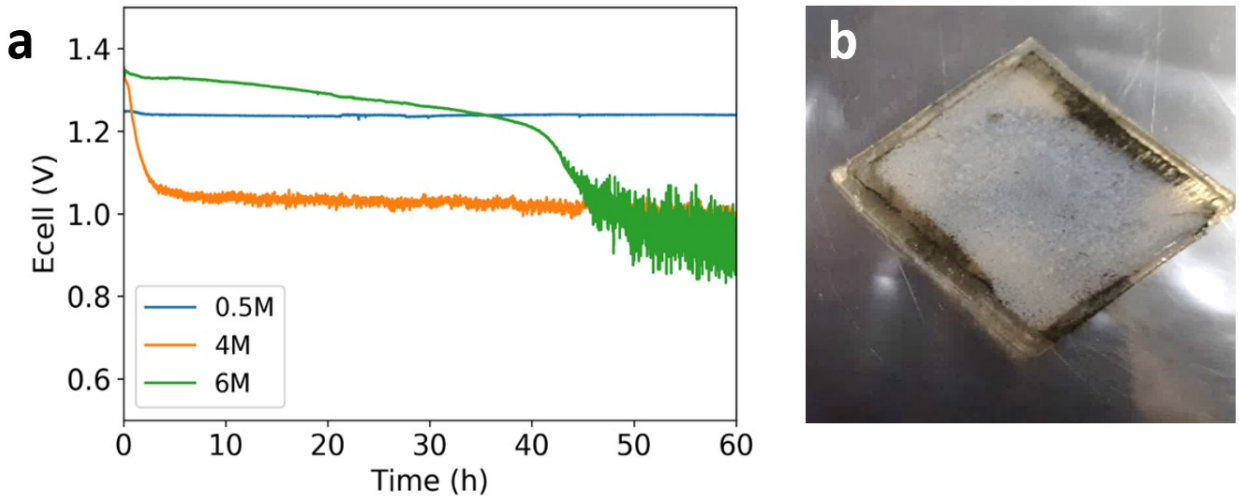

Figure S19 – a) OCV stability for various NH_4Cl concentrations of [C/MnO_2/GPE#2[NH_4Cl]/Zn/C] cells; b) Image of 4M NH_4Cl GPE#2 electrolyte layer on top of a Zn anode (on carbon substrate) after 50 h, with clear visible white precipitate forming at the interface.

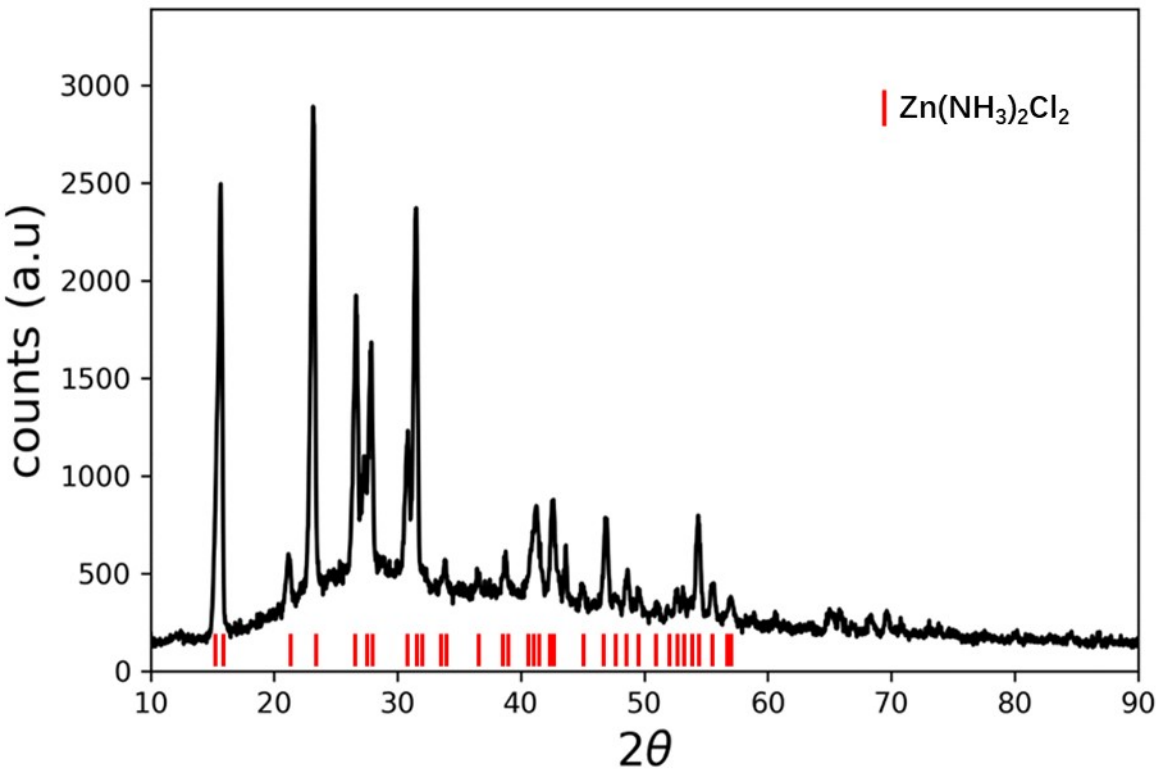

Figure S20 – X-ray diffraction pattern of the white precipitate present at the Zn/GPE#2 interface. The indices correspond unequivocally to $Zn(NH_3)_2Cl_2$.

The formation of $Zn(NH_3)_2Cl_2$ occurs through the following reaction:

$$ZnO(s) + NH_4Cl(aq) \rightleftharpoons Zn(NH_3)_2Cl_2 + H_2O$$

A layer of oxide is always present at the surface of metals, and the presence of ZnO is therefore impossible to avoid. This is a known problem in the aqueous Zn-cells, and attempts have been made to remove ZnO from Zn particle surfaces to prevent the formation of unwanted precipitate [34]. While removal of ZnO from the system is one method to prevent the $Zn(NH_3)_2Cl_2$ formation, this was not considered practical in an aqueous based electrolyte, since the ZnO would inevitably reform. Interestingly, when a low surface area Zn metal sheet was used as the anode, the formation of $Zn(NH_3)_2Cl_2$ was negligible enough so as to not alter the electrochemical stability of the system (**Fig. S21**). However, screen-printed electrodes are made of high surface Zn particles (5-30 µm particle size), which generated a significant concentration of $Zn(NH_3)_2Cl_2$, resulting in the observed instability.

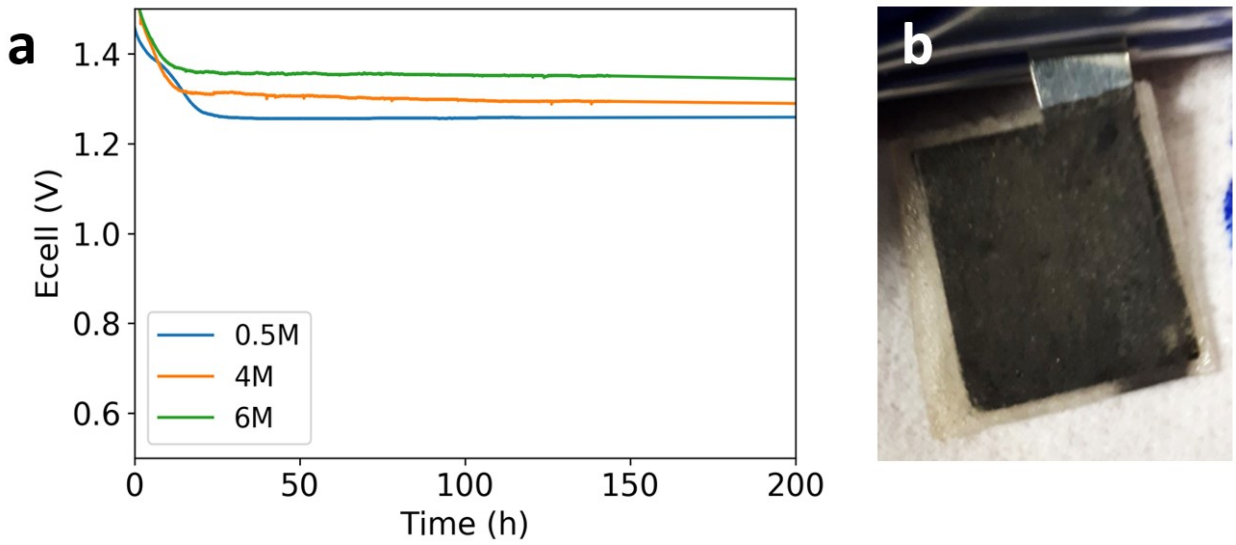

Figure S21 – a) Cell voltage stability for various NH_4Cl concentrations of [C/MnO_2/GPE#2[NH_4Cl]/Zn flat plate] cells; b) Image of 6M NH_4Cl GPE#2 electrolyte layer on top of a Zn flat plate after 200 hours at OCV, showing negligible precipitate formation.

To mitigate this issue, an electrolyte formulation was developed that inhibits the formation of $Zn(NH_3)_2Cl_2$. It was found that $Zn(NH_3)_2Cl_2$ can be "buffered" in the system to remain soluble during the lifetime of the cell [35-39]. Since $Zn(NH_3)_2Cl_2$ is more soluble in acidic conditions, both control of the pH and addition of $ZnCl_2$ helped prevent the precipitation of $Zn(NH_3)_2Cl_2$. $ZnCl_2$ is able to buffer the solution through its reaction with chloride ions, helping to maintain $Zn(NH_3)_2Cl_2$ as a solubilized salt, according to the following equilibrium reactions:

$$ZnCl_2 + 2Cl^- \rightleftharpoons ZnCl_4^{2-}$$

$$Zn(NH_3)_2Cl_2(s) \rightleftharpoons Zn(NH_3)_2^{2+}(aq) + 2Cl^-(aq)$$

This concept was confirmed experimentally, as presented in **Figure S22**. In this experiment, 10 mL electrolyte solutions were titrated with increasing quantities of ZnO, until a precipitate was formed (confirmed to be $Zn(NH_3)_2Cl_2$). In the case of pure NH_4Cl, precipitation occurred after 150 mg addition of ZnO, which corresponds to a solution pH of ~6.5-7. However, with a mix of NH_4Cl:$ZnCl_2$ in a 75:25 weight ratio, the solution was able to accommodate much larger amounts of ZnO, as well as maintain a more stable pH range before precipitation occurred. In all instances, the precipitate formed at the onset of pH ~6.5. The system was independent of actual total concentration, with the critical component being the NH_4Cl:$ZnCl_2$ ratio[24,28].

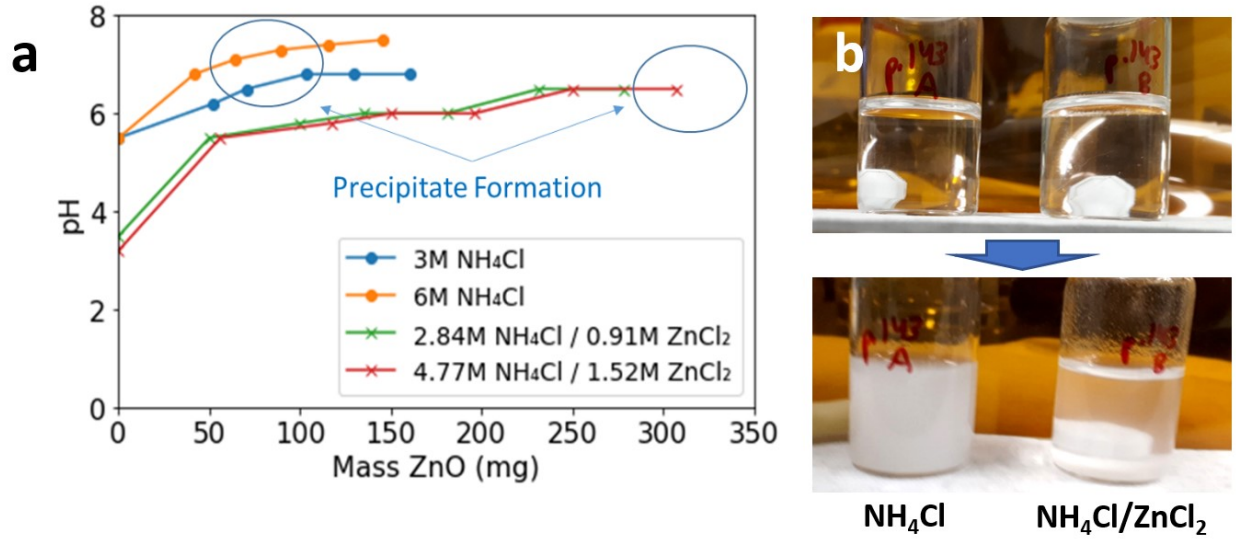

Figure S22 – a) Solution pH vs. added ZnO. Circles indicate approximate range of initial precipitation; b) Photographs of initial and final solutions after precipitation occurred for 3M NH_4Cl and 2.84M NH_4Cl/0.91M $ZnCl_2$.

Based on these results, various electrolytes along the 75:25 ratio were tested with GPE#2. Perfectly stable OCV was observed for all cells assembled with such electrolytes, with no precipitation of $Zn(NH_3)_2Cl_2$ for extended periods of time (months). 2.89M NH_4Cl + 0.91M $ZnCl_2$ was chosen as the optimal electrolyte concentration, as higher concentrations resulted in "salting-out" issues as well as poor mechanical integrity of the final polymer electrolyte.

4-3) Development of GPE#3 (PVA-*g*-PCL)

The idea was to develop a fully biodegradable GPE that could take advantage of the previously demonstrated UV-curable acrylate functionalities, leading to fast solidification of the formulation after printing. It was understood from the GPE#2 development that the block PCL was advantageous to control the mechanical properties of the polymer by varying the length of PCL blocks, thanks to its natural stiffness. PCL chains can develop from the hydroxyl groups along the PVA chain via ring-opening polymerization (ROP) of the caprolactone monomer. It is worth noting that PVA is first created as PVAc (polyvinyl acetate), and then selectively hydrolyzed to varying degrees. The degree of hydrolysis of PVA influences its water solubility in a counterintuitive manner. Indeed, the higher the hydrolysis degree, the lower the solubility, because of chain folding and the formation of folded hydrogen-bounded aggregates. Since PCL is insoluble in water, it was decided to choose a PVA with a low degree of hydrolysis, to help maintain a good water solubility of the copolymer.

4-3-1) Two-step synthesis of the acrylated PVA-g-PCL

Step 1:

To a 500 mL 2-necked round-bottomed flask was added a medium football-shaped stir bar, followed by 20 g PVA (Sekisui Poval 5-74, Mw~10K, 452 mmol, 74% hydrolyzed). The flask was connected to a vacuum line, and heated to 100°C with stirring for 30 minutes to remove water (material remained a dry powder during the drying). The vacuum line was replaced with a N_2 purge line, the flask was cooled to 70 °C and 80 mL of dry distilled DMSO was added via syringe, then the reaction was reheated to 100 °C and stirred for approximately 2 h until the PVA was completely dissolved. Next, the reaction was cooled to 90 °C, and 25.16 mL of distilled e-caprolactone (26 g, 226 mmol, 0.5 eq.) was added via syringe, followed by 160 µL tin (II) 2-ethylhexanoate catalyst. Finally, the reaction was heated to 100 °C and allowed to run overnight.

The reaction mixture was pale golden. Heating was stopped, and the reaction was allowed to cool to room temperature, forming a viscous syrup. The reaction contents were poured in two portions into two 2L beakers, each containing 1 L of stirred isopropyl alcohol (IPA). A white jelly flocculated solid formed immediately. The IPA suspension was transferred to plastic centrifuge bottles and the solid was isolated via centrifugation at 2,000 rpm for 15 min. The clear supernatant solution was poured off and discarded and the soft spongy solid mass of polyol was then transferred to a recrystallization dish to dry overnight at ambient temperature. A small portion of the material was isolated and oven dried at 70 °C and checked by ^{1}H NMR in D_2O. The remainder of the semi-dried cheese-like polymer gel was dried in the oven overnight to remove the residual IPA. The material became tough and leathery in the oven, but cooled to a tough, semi-brittle beige polymer. Finally, the dried solid polyol was pulverized in a coffee grinder to furnish 19 g of amber granular solid polyol.

Step 2:

To a 250 mL 1-necked round-bottomed flask was added a medium football-shaped stir bar, followed by 3.0 g PVA-g-PCL polymer. Next, 100 mL of anhydrous DMF was added via syringe, and the flask was heated to 40 °C with stirring. After 3 h of mixing, the material was completely dissolved to form a pale golden solution. Next, 0.41 mL of triethylamine (TEA) (0.3 g, 10 wt.%) was added followed by 0.27 mL (0.3 g, 10 wt.%) acryloyl chloride (dropwise). No visible changes were observed. The reaction was allowed to stir overnight at 40 °C, no protection from light was provided. Again, the reaction was unchanged in appearance. The reaction was removed from heat and allowed to cool to room temperature. The reactor contents were poured into 1 L of rapidly stirred IPA, forming a cloudy white solution with fine soft flocculated solid. The mixture was stirred for 30 min, then transferred to plastic centrifuge bottles and centrifuged at 2,000 rpm for 15 min, supernatant was removed, and the settled macromonomer jelly was rinsed with 200 mL of fresh IPA and centrifugation was repeated. Soft opaque white jelly settled on bottom of bottles. The IPA supernatant was poured off and discarded, and the settled soft white opaque jelly product was transferred to an amber glass jar, sealed with parafilm, and stored in the fridge.

The intermediate polyol was characterized by ^{1}H NMR to determine the DP (degree of polymerization) and the % PCL content (see **Fig. S23**). This was achieved through end group analysis and integration of the signal at 3.65 ppm (ω', CH_2 group adjacent to terminal OH of PCL), 3.5 ppm (ω, CH_2 group adjacent to ester O of PCL), 2.35 ppm (α-CH_2 groups of repeat and terminal PCL chains), and 2.0 ppm (residual acetate groups of PVA). Calculations to determine the degree of polymerization (DP) and PCL content were done by measuring the relative integrals of the CH_2 groups beside the repeat ester unit and terminal OH groups (at 3.5 and 3.6 ppm, respectively), as follows:

- DP = ω/ω'
- PCL:PVA = (α,α')/2:acetate/3(0.3)

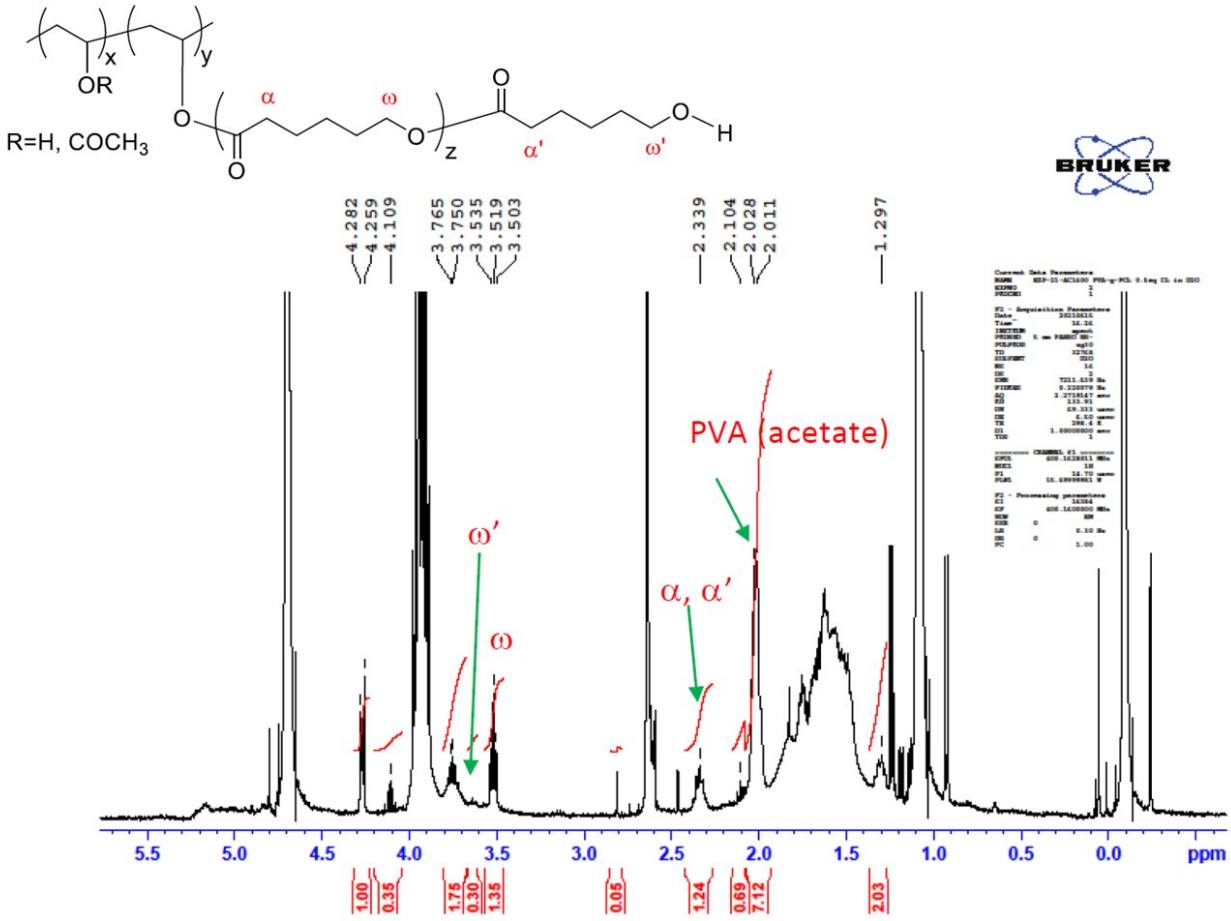

Figure S23 – ^{1}H NMR characterization of the intermediate graft copolymer.

The ^{1}H NMR spectrum of the final acrylated graft copolymer (**Fig. S24**) clearly shows the acrylate peaks. The degree of conversion of OH groups to acrylates was not quantified, due to the complexity of overlapping signals. Note the shift of the ω' terminal CH_2 of acrylate product to 3.2 ppm (from 3.65 ppm) when the OH group is converted to an acrylate ester.

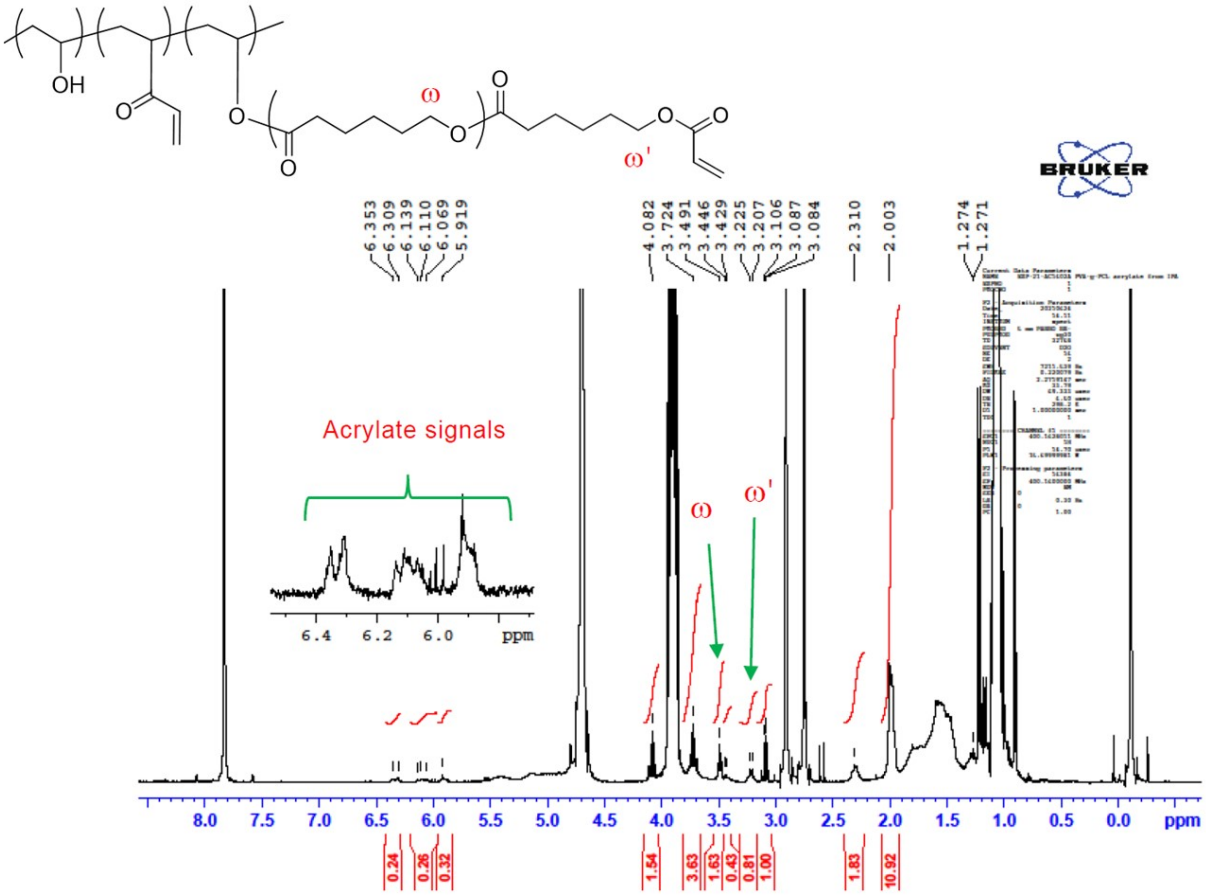

Figure S24 – ^{1}H NMR characterization of the acrylated graft copolymer.

Multiple conditions were tested to optimize the properties of GPE#3. **Figure S25** shows the results of a study where the starting CL:PVA ratio was varied. Experiment 1 led to a soft and elastic gel, that did not have sufficient toughness for the application (Young's modulus of 0.11 MPa) whereas Experiment 3 provided a stiff and brittle polymer gel electrolyte with a Young's modulus of 0.3 MPa. The GPE#3 produced using the copolymer of Experiment 2 proved to possess the proper combinations of mechanical properties for a battery polymer gel electrolyte (Young's modulus of 0.11 MPa). Since PCL is a stiffer polymer compared to PVA this result can seem to be counterintuitive. A possible explanation is that increasing the amount of PCL side-chains decreases the occurrence of short links between neighboring PVA chains (occurring at sites where the acrylate function has been grafted directly onto the main chain) thereby increasing chain mobility.

Conductivities of the GPE#3s, all in a fairly narrow range (46-72 mS/cm), showed an opposite trend compared to the Young's modulus, the more elastic variation showing the highest conductivity. These results can be expected, since the mechanical properties of the polymer matrix are not critical factors for ion mobility in a gel-type electrolyte, but stiffness can still slightly impede mass transfer. Further optimization experiments suggested that the suitable range for the application (combining both appropriate mechanical properties and ionic conductivity) was between 4 and 7 wt% PCL content in the copolymer.

a

Experiment	CL:PVA (mol)	DP	PCL:PVA	wt% PCL
1	1.0	3.64	1:7.7	11.5
2	0.5	2.47	1:15.8	5.95
3	0.25	0.84	1:51.4	1.9

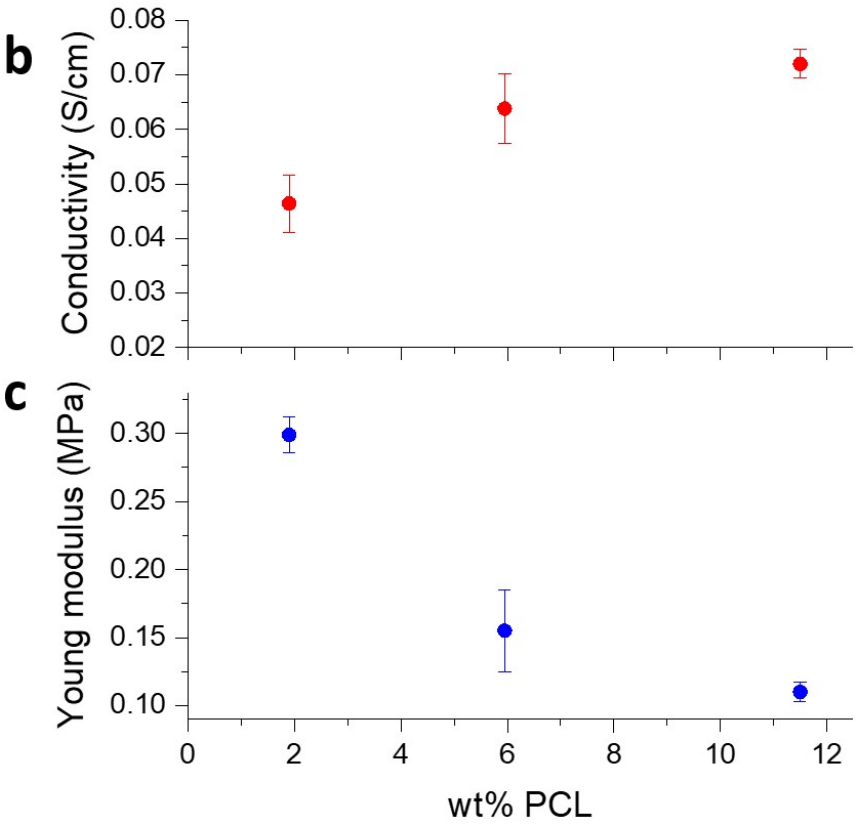

Figure S25 – a) Table showing the resulting PCL content and DP for different CL:PVA ratios; Ionic conductivity (b) and Young's modulus (c) of the corresponding GPE#3.

4-3-2) One-pot synthesis of the acrylated PVA-g-PCL

In order to bypass the long and troublesome isolation, purification and drying steps of the intermediate polyol, a one-pot protocol was developed later on, which proved to be more efficient and yielded products of equivalent quality. DMSO, NMP and DMF were tried out as solvents for the two steps and each proved to yield products with similar quality. DMF was finally chosen for its lower boiling vs. NMP or DMSO, in order to facilitate solvent removal.

Besides, it was found that IPA did not precipitate the acrylated copolymer efficiently, forcing the use of methods such as centrifugation and solvent decanting. A precipitation study was therefore performed with a number of solvents to improve the material's recovery process. A 3:1 mix of acetone and dichloromethane (v:v) was found to allow the isolation of the material as a glassy solid product without the need for centrifugation. These combined improvements are detailed in the procedure below:

One-pot procedure with mixed solvent precipitation method:

To a 250 mL 3-neck round-bottomed flask was added a medium football-shaped stir bar, followed by 20.0 g PVA (Sekisui Poval 5-74, Mw~10K, 74% hydrolyzed). The flask was purged with argon, then heated to 100 °C. Once 100 °C was reached, 50 mL of NMP was added. After 1 h, once the PVA had fully dissolved, 25.1mL of caprolactone (25.1 mL) was added, followed by dropwise addition of 0.16 mL Sn(II) 2-ethylhexanoate. The reaction was allowed to stir overnight at 100 °C. The reaction solution had gained a more intense yellow color, though it was still clear. The reaction temperature was lowered to 80 °C and then 0.83 mL of triethylamine (0.60 g, 5 wt%) was added followed by a dropwise addition of 0.54 mL acryloyl chloride (0.60 g, 5 wt%). The reaction was allowed to stir overnight at 80 °C.

The reaction was removed from heat and allowed to cool to room temperature. The reactor contents were poured into a 3:1 acetone:DCM mixture chilled to 5 °C and gently stirred, upon which spaghetti-like strands of precipitated product formed. The product was filtered out and dried at room temperature, then under vacuum at progressively increased temperatures, to remove traces of DMF and unreacted caprolactone. An off-white glassy solid was finally obtained.

4-3-3) One-pot synthesis scale-up

The synthesis was subsequently upscaled to 4 L batches as follows: A 4 L glass reactor was purged with N_2 and then charged with 1706.4 g of DMF. The reactor was set to 150 rpm mixing speed and a temperature of 100 °C. 360 g of PVA was then added and mixed for 1 h for complete dissolution. An emulsion of 6.98 g Sn(II) 2-ethylhexanoate catalyst in 464 g caprolactone was prepared and added over a period of 1 min. The reaction was allowed to proceed for 5 h at 100 °C while mixing at 150 rpm. The reactor was then cooled to room temperature (25 °C) and hold overnight without mixing under N_2 flow.

The obtained gelled mixture was heated to 60 °C while mixing at 150 rpm intermittently. Once the gel has turned into a viscous liquid, the reactor was cooled 40 °C. 10.77 g of triethylamine base was then added and mixed for 15 min. A solution of 10.88 g acryloyl chloride in 51.19 g DMF was then prepared and added to the reactor while maintaining the temperature < 60 °C. The reaction proceeded for 4 h at 40 °C. At the end of the reaction, a larger 6 L reactor was charged with the precipitation solvent (a premixed 3:1 v:v acetone:DCM mixture), and chilled to 5 °C using a water/ice bath. The 4 L reactor containing the DMF solution of the reaction product was discharged hot into a pail, and then transferred via peristaltic pump into the chilled 6 L reactor with gentle mixing, upon which spaghetti-like strands of precipitated product formed. Since the product is highly compressible and could not be discharged via the bottom valve, only the precipitation solvent was drained out. The product was isolated manually by removing the reactor dome and filtered using Clear Edge PTFE cloth then transferred to foil pans to dry first at room temperature. Once the air-drying process was completed, the product was then vacuum oven dried to furnish an off-white glassy solid. **Figure S26** shows images of the scale-up synthesis at different stages.

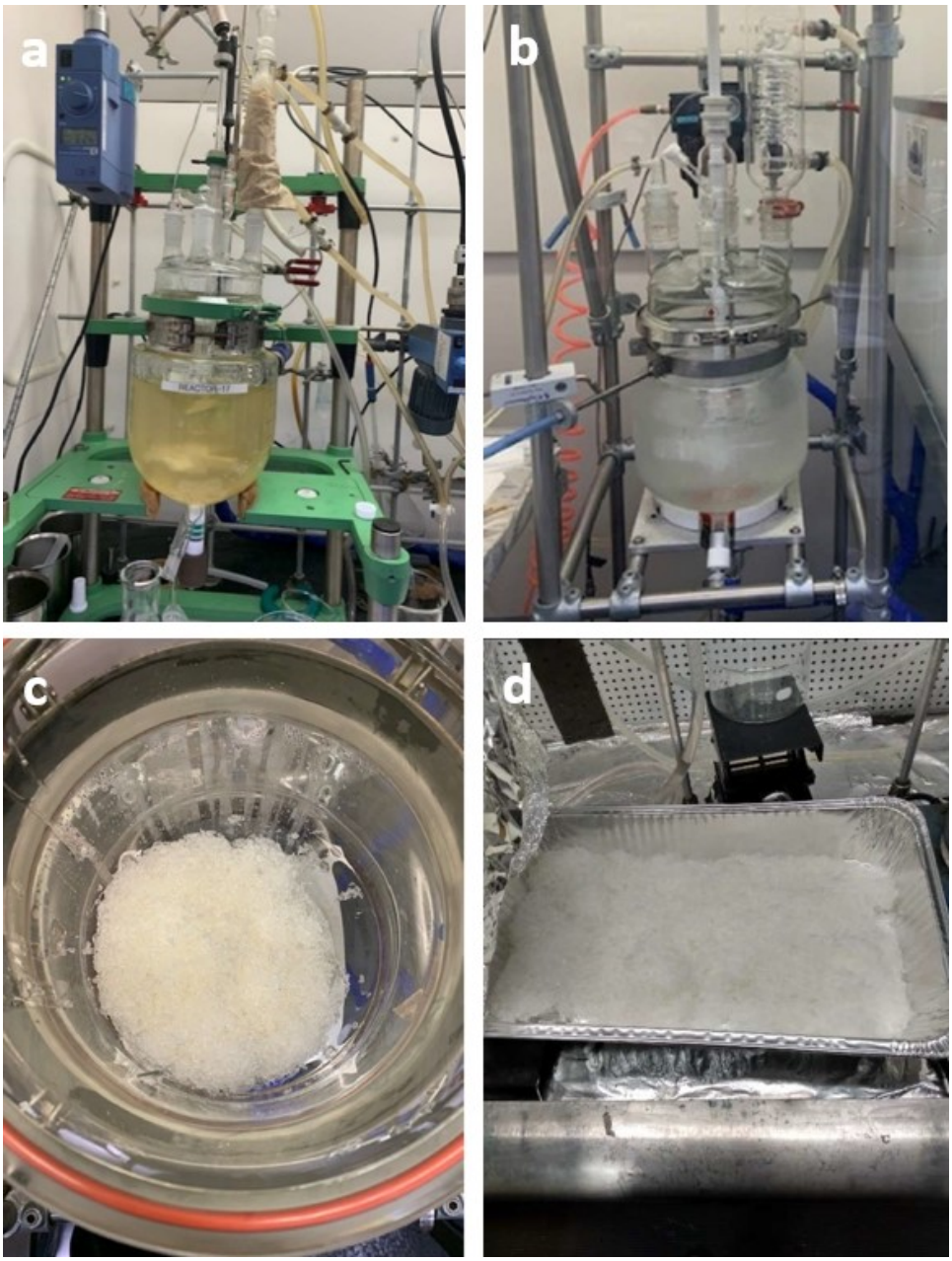

Figure S26 – Scale-up synthesis with large reactors. a) 4 L reactor; b) 6 L precipitation reactor; c) Rubbery precipitate after solvent removal; d) Pan-drying of precipitated product.

4-3-4) Electrolyte ink formulation

Polymer electrolyte inks were obtained by dissolving typically 20 wt% GPE#3 and 0.1 wt% LAP photoinitiator (lithium phenyl-2,4,6-trimethylbenzoylphosphinate) in an already prepared electrolyte solution (2.89M NH_4Cl + 0.91M $ZnCl_2$ in H_2O). The solution was magnetically stirred for at least 2 h before printing.

SECTION 5: BATTERY PRINTING AND ASSEMBLY

Battery fabrication was carried out using a multi-step printing process shown in **Fig. S27**, using a manual screen-printer (ASC2420, **Fig. S28a**) and custom-designed screens. Electrodes were produced in 3x3 arrays.

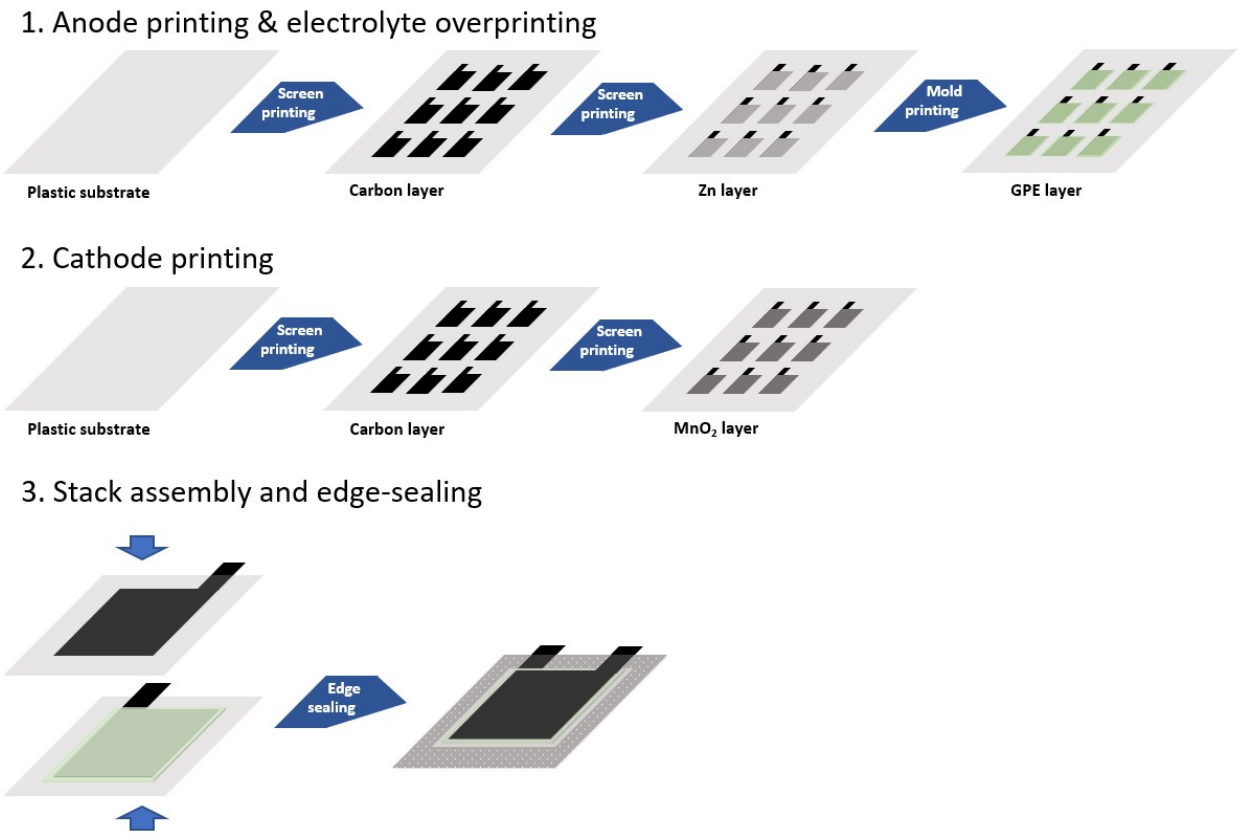

Figure S27 – Step-by-step battery fabrication process.

The screens were prepared using diazo emulsion. The light-sensitive emulsion was coated on both sides of a screen and dried in air. A stencil design was created using GIMP software and printed on transparent PET sheets. The stencil sheet was placed on top of the dry emulsion-coated screen as a shadow mask. The screen was then exposed to UV irradiation using a broadband UV lamp to create the desired pattern on the screen (negative resist). The unexposed areas (not crosslinked) were washed out of the screen with water and an aperture pattern of the desired print image was thereby created. Different screens were created for the various battery layers, as shown in Fig. S26. 180, 80 and 60 mesh screens gave thicknesses of ca. 20 µm, 40 µm and 60 µm, respectively.

During process development, both polyethylene terephthalate (PET) substrates (non-biodegradable) or PLA substrates were used, the latter being either the PLA-D grade developed in Section 2.1 or a commercial grade aluminized PLA (Celplast ENVIROMET). The battery substrate was secured onto the

screen printer bed using Kapton tape at the corners and edges. The stenciled screen was then placed over the substrate with the inkwell side up, and lined up to the desired print area. The screen was then secured using the screw clamps. The carbon current collector paste ink was then poured onto the top edge of the screen and then a 60-80 durometer squeegee was used to pull the ink down across the stencil to push ink through the stencil and onto the substrate below. The wet print was placed in an oven at 140 °C for 9 min to dry the carbon current collector prints, which yielded a ca. 6 µm thick dry layer of conductive carbon.

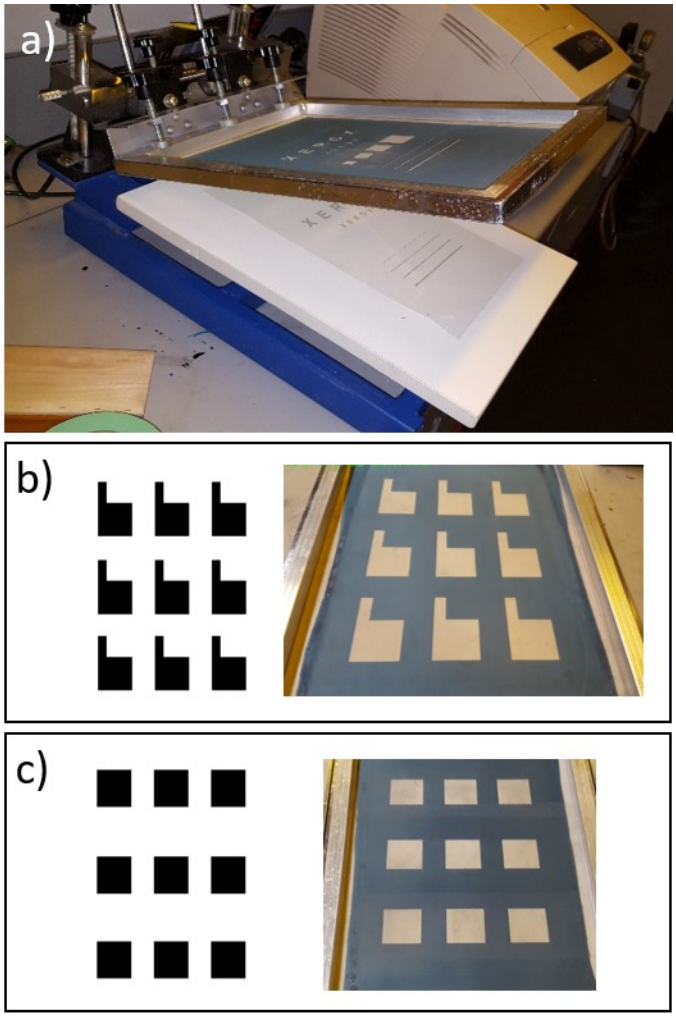

Figure S28 – a) Picture of the ASC2420 manual screen-printer; b) Current collector layer stencil design and the resulting mesh imaged screen; c) Active layer stencil design and the resulting mesh imaged screen.

The active layer stenciled screen was then placed over the current collector printed substrate, inkwell side up, and lined up by eye such that the stencil pattern aligned with the desired active layer print area on the current collectors. Masking tape was place around all edges of the ink-well side. The printing of the Zn and MnO_2 active layers was carried out similarly as for the current collector layer, with

adjustments in the squeegee angle and force depending on the rheological properties of the inks. The printed inks were dried for 9 min at 140 °C.

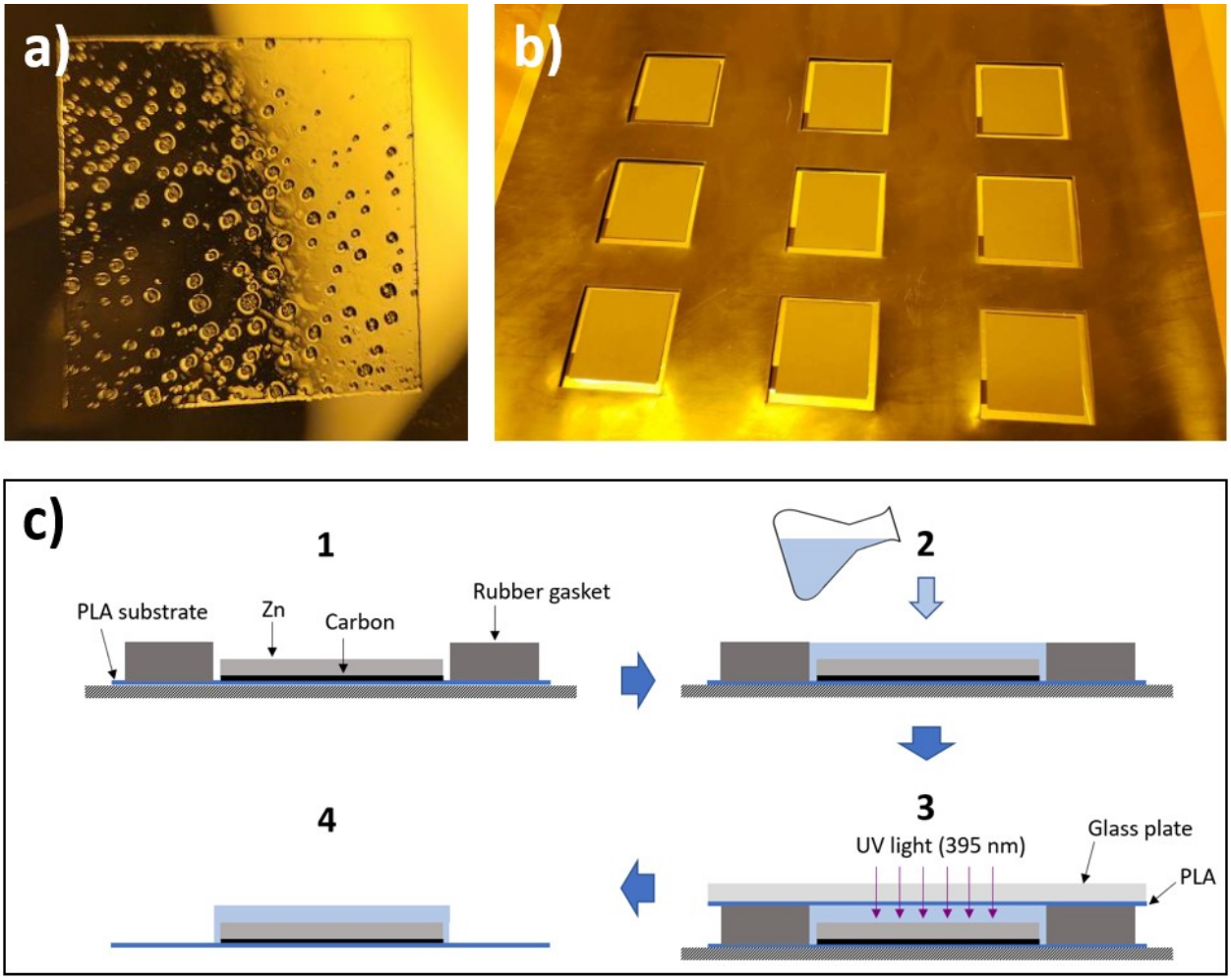

Figure S29 – a) Picture showing the typical bubbling issues occurring during the GPE layer screen-printing; b) Picture of the rubber gasket placed over the Zn electrodes; c) Mold printing process. 1) a rubber mold is placed over the electrodes; 2) a quantity of GPE precursor solution is poured in each cavity; 3) a PLA sheet and a glass plate are placed on top and UV is used to cure the GPE; 4) Mold-printed GPE layers are obtained after removal of the glass plate, PLA sheet and mold.

Screen-printing of the GPE proved to be challenging with significant bubbling caused by the screen (**Fig. S29a**). An alternative method based on molding was therefore developed to obtain a bubble-free and thickness-controlled layer of electrolyte (**Fig. S29b-c)**. A 700 µm thick rubber gasket was cut to the required dimensions, and its internal edges were wiped with a silicone glycol copolymer (Silsurf A208 from Siltech) to help with the mold release. The mold was placed over the electrodes, then each cavity was filled with a selected quantity of GPE precursor solution. A PLA sheet was then rolled over the mold in order to eliminate entrapped air pockets, then a glass plate was placed on top with sufficient pressure to seal the gasket and spread the polymer electrolyte solution evenly into the mold cavities. The GPE was cured using a Phoseon 16W 395nm LED lamp at 10-inch height for 1000 milliseconds. The mold-

printing technique enabled the formation of GPE layers of controlled thickness with excellent reproducibility.

a **Optimal battery characteristics**

Component	Thickness (mm)	Weight (g)	Details
Substrate/packaging	0.12	0.765	PLA-D/Al laminate 5.5 x 5.5 cm^2 (*x2*)
Current collectors	0.006	0.031	Nagase ChemteX Cl-2042 (*x2*)
Cathode active layer	0.08	0.788	MnO_2:graphite:alginate (79:20:1); 4 x 4 cm^2
Anode active layer	0.025	0.257	Zn:alginate (99:1); 4 x 4 cm^2
Electrolyte	0.1	0.382	GPE#3 [$ZnCl_2$:NH_4Cl]; 4.5 x 4.5 cm^2
TOTAL	**0.46 mm**	**3.02 g**	

Optimized features:

- Doubling of MnO_2 (80 µm active layer)
- Stoichiometric excess of Zn vs MnO_2 decreased from 41 % to 10 %
- Packaging serves as substrate; dimensions decreased from [7x7] to [5.5x5.5] cm^2
- Packaging thickness decreased to 120 µm PLA_{int}/Al/PLA_{ext} (80:20:20)
- GPE layer's thickness decreased to 100 µm

b

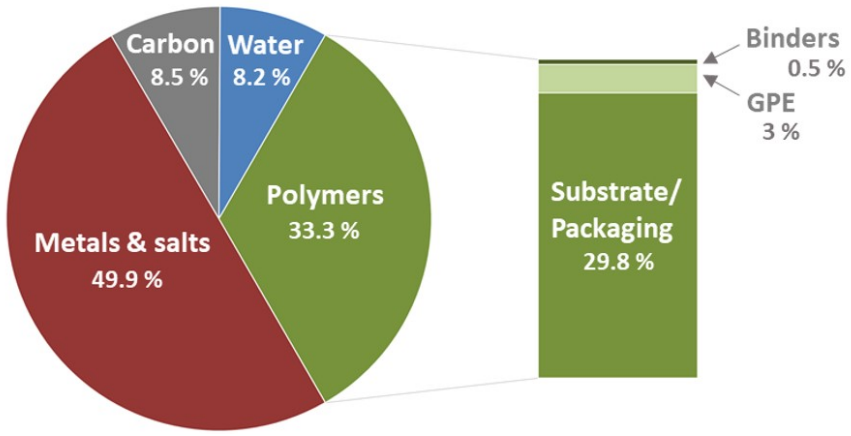

Figure S30 – Possible scenario of optimization for a compostable Zn-MnO_2 cell.

SECTION 6: PERFORMANCE TESTING

Figure S31 – Picture of Molex cells (Product # 133310001), purchased 06/2024.

OCV (V)	OCV (V)	Area (cm²)	Current (mA)	Capacity (mAh)	Areal capacity (mAh/cm²)	Areal energy (mWh/cm²)
NRC (this work)	1.4	16	0.7	95 ± 5	5.9 ± 0.3	6.2 ± 0.3
Molex	1.5	25	1/1.09	90/38[1]	3.6/1.5[1]	4.3/1.8[1]
Blue Spark	1.5	16.5	1-2	10	1.65[2]	2.0[2]
Enfucell	1.5	19.8	1	40	2.02	2.63
Imprint Energy[3]	1.5[3]	21.25	1	15[3]	0.71[3]	0.85[3]

[1] Claimed cell capacity (datasheet) / average capacity measured on 5 cells at 1.09 mA.

[2] The datasheet notes that this is the 'input capacity' and that output capacity is greatly determined by the operating conditions.

[3] Information provided on a 3 V battery (2 cells connected in series). Data was extracted and calculated to represent a single cell given the principles of capacity, current and voltage for batteries connected in series.

Table S4 – Characteristics of the compostable cell and commercially available printed Zn/MnO_2 cells.

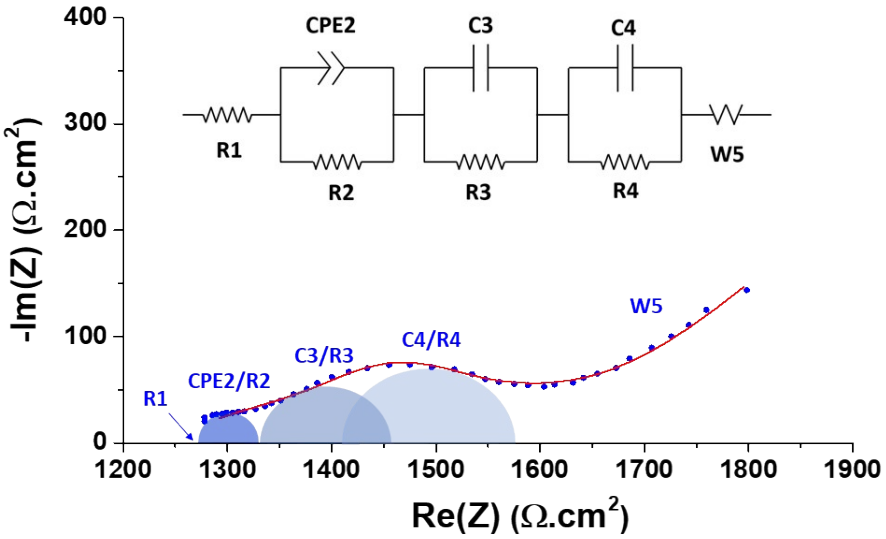

R1: high frequency resistance (internal resistance)

R2/CPE2: resistance and constant phase element related to a 1st MnO_2 electrochemical process

R3/C3: resistance and capacitance related to a 2nd MnO_2 electrochemical process

R4/C4: resistance and capacitance related to the Zn electrochemical process

W5: Warburg diffusion resistance at the vicinity of the electrodes

Figure S32 – Typical impedance Nyquist plot of a Leclanché cell and the equivalent circuit used to model the curve. The blue dots are the real data and the red curve is the fitting using the equivalent circuit.

Constant phase elements (CPEs) are typically used in replacement of pure capacitance to model highly porous electrodes. In this case, only by using a CPE to model the first MnO_2 process was it possible to obtain satisfactory fitting curves. The reason is unknown and its investigation would require further electrochemical experimentations which are beyond the scope of this investigation.

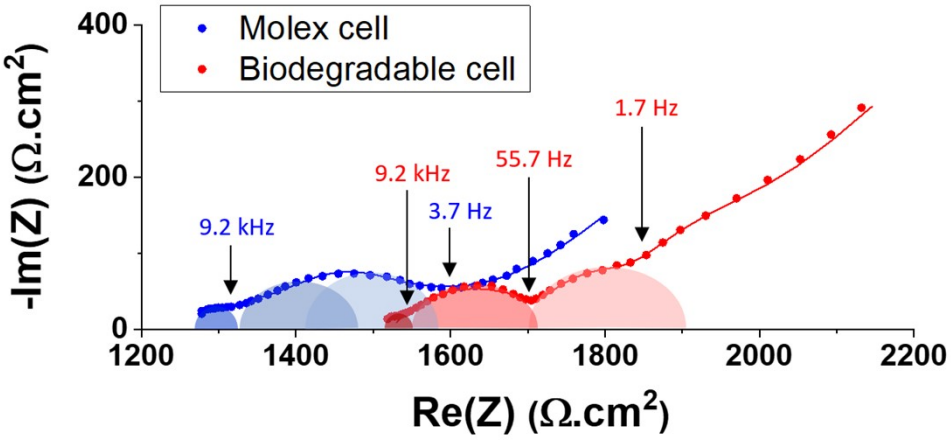

Figure S33 – Nyquist plot of the compostable and Molex cells, including the frequency of inflexion points.

Three semi-circles can be observed on Fig. S33 in the case of the biodegradable cell, whereas only two processes are distinguishable for the Molex cell. However, it is likely that two of the resistive processes are convoluted into a single larger semi-circle, as illustrated by the colored half-disks represented under the curve. Analysis of the frequencies of the charge-transfers also point to this conclusion: the first and third inflexions points are similar for both cells, and the second inflexion of the compostable cell has an intermediate frequency, suggesting that this process is convoluted into the large second semi-circle of the Molex cell. Moreover, the fitting of the curves was only successful when considering three processes (equivalent circuit shown in Fig. S32). Even though the exact determination of the electrochemical processes of a Leclanché cell has never been clarified, it is generally considered that the process occurring at the lowest frequencies is the Zn electrochemistry whereas the two other processes are occurring on the MnO_2 electrode [40].

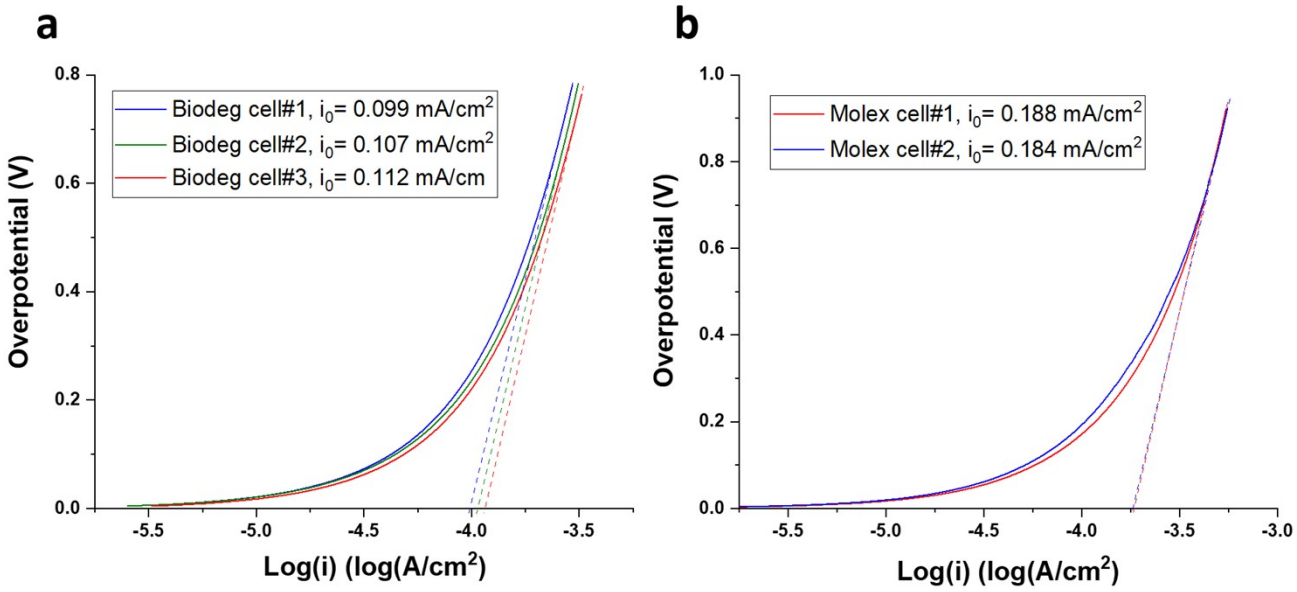

Figure S34 – Tafel plots of biodegradable (a) and Molex (b) cells. The exchange current density i_0 is determined by the extrapolation of the current at 0 V of overpotential.

The apparent exchange current density (i_0) can be derived from the Tafel plots, using the Tafel equation:

$$\eta = \left| A log\left(\frac{i}{i_0}\right) \right|$$

where η = overpotential (E − OCV)

A = Tafel slope

i = current density

i_0 = exchange current density

Here, i_0 is different from the true exchange current density of the individual half-cell reactions, but represents an apparent open-circuit extrapolated current (Fig. S34). This measures an overall cell kinetic response to overpotential (meaning power demand).

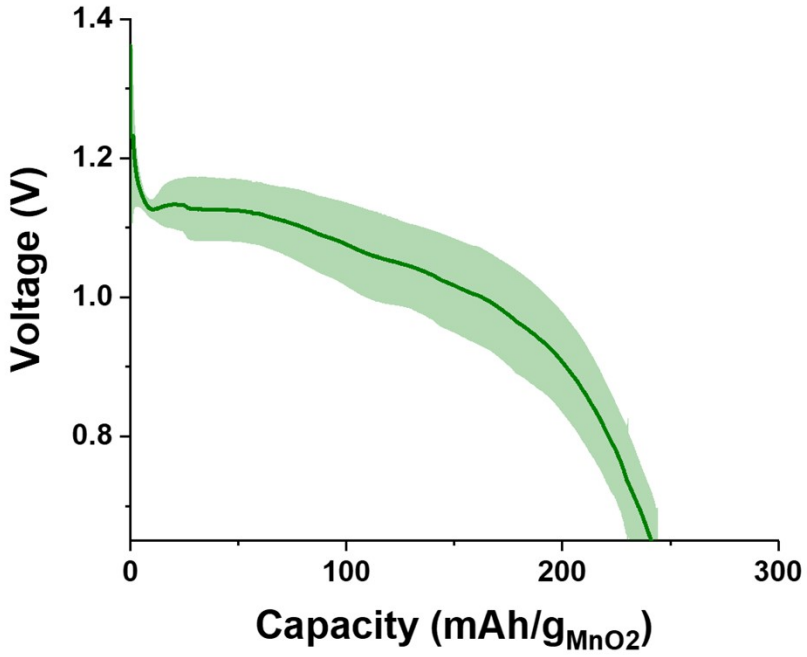

Figure S35 – Discharge curve of the biodegradable cells at 0.7 mA. Capacity per mass of limiting active material (MnO_2).

SECTION 7: COMPOSTABILITY TESTING

7-1) Methodology

The ASTM D5338 protocol was used under the guidelines of the ASTM D6400 method. This procedure has been developed to permit the determination of the rate and degree of aerobic biodegradability of plastic products when placed in a controlled composting process. This standard is equivalent to European norms EN 13432 and ISO 14852. Here is a series of notes clarifying and defining certain conditions, parameters and limitations:

1. The ASTM D5338 determines the degree and rate of aerobic biodegradation of plastic materials on exposure to a controlled-composting environment under laboratory conditions. The materials are exposed to (buried into) an active compost obtained from an industrial solid waste facility. The aerobic composting takes place in an environmental growth chamber (reactor) where temperature, aeration and humidity are closely monitored and controlled.
2. This test method is designed to provide reproducible and repeatable test results under controlled conditions that resemble composting conditions. It is designed to yield a percentage (%) of conversion of carbon (C) in the sample into CO_2. The carbon that has been converted into CO_2 through biodegradation reactions (either through biotic chemical reactions or a combination of biotic and abiotic reactions) is called “mineralized carbon”.
3. This test method is designed to be applicable to all plastic materials that are not inhibitory to the microorganisms present in aerobic composting piles.
4. The ASTM D5338 is a protocol describing a methodology, but ASTM D6400 is the guideline that defines a series of criteria and tests to be conducted along this protocol in order to certify the compostability of the tested material, namely:
    - Effective disintegration in the compost (absence of debris),
    - Demonstration of inherent biodegradation,
    - Absence of adverse impacts on the ability of compost to support plant growth (absence of eco-toxicity and low heavy metal content).
5. Because there is a wide variation in the construction and operation of composting systems and because regulatory requirements for composting systems vary, this procedure is not intended to simulate the environment of any particular composting system. However, it is expected to resemble the environment of a composting process operated under optimum conditions. More specifically, the procedure is intended to create a standard laboratory environment that will permit a rapid and reproducible determination of the aerobic biodegradability under controlled composting conditions.

7-2) Experimental setup

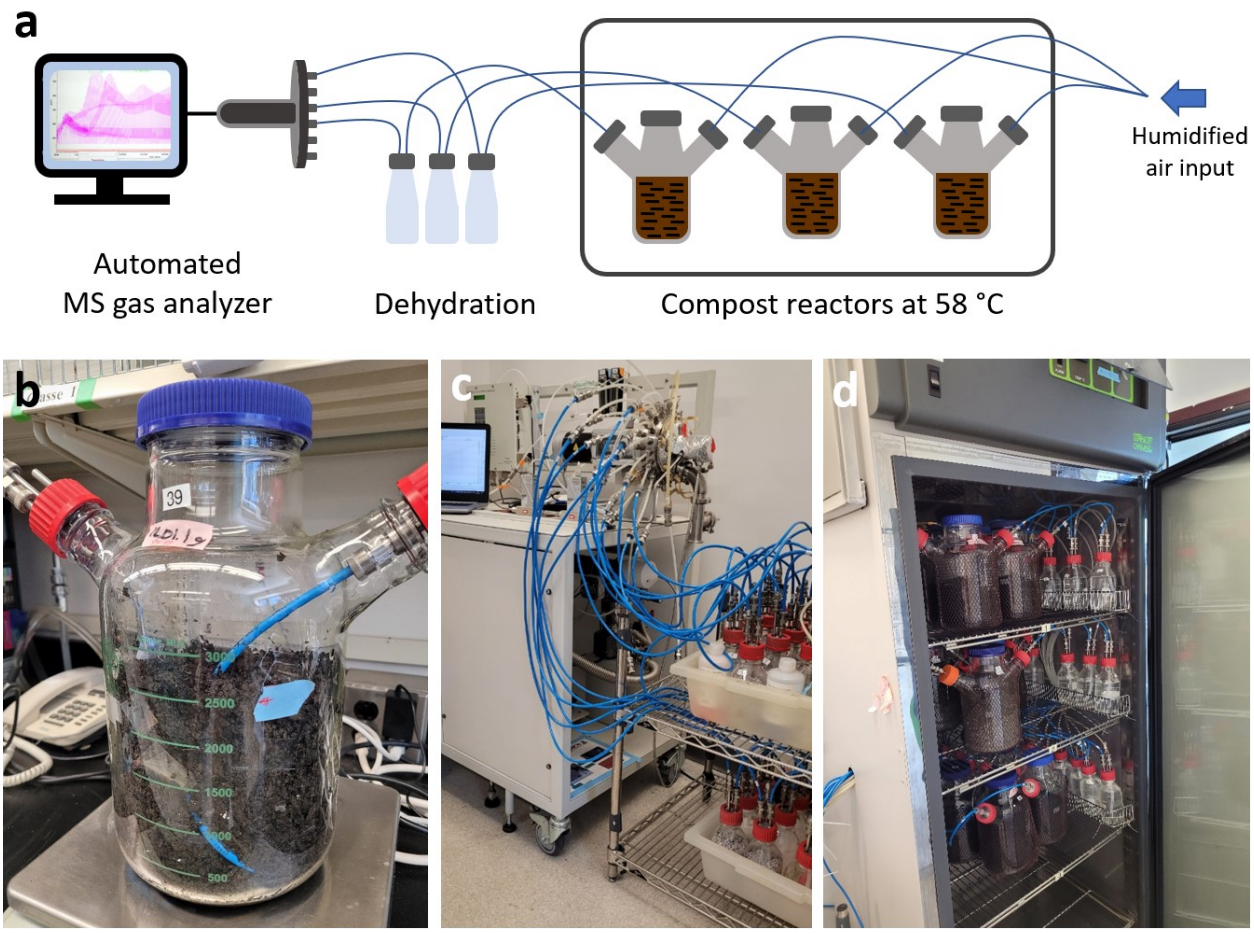

Figure S36 – Compostability testing setup. a) Schematic representation of the composting setup including a mass spectrometer analysis system (QIC BioStream™ from Hiden Analytical); b) composting reactor; c) Picture of the Proteus multi-stream gas valve of the QIC Biostream system; d) Picture of the Caron 6030 environmental chamber with 18 reactors.

The composting testing setup is schematized in **Fig. 36a**. It comprised a temperature controlled environmental chamber (Caron 6030), an air humidification column at the inlet, 18 rotameters (0 – 60 mL/min), 18 glass bioreactors (6 L), and 18 glass water condensers (1 L) at the outlet, all of which were interconnected using Teflon tubes (¼ inches diameter). Air tightness of all bioreactors was checked before the start of all tests. To maintain aerobic conditions, air flow rate was set at 50 mL/min and humid air was forced to flow through the compost by means of a perforated Teflon tube (¼ inch diameter). Once the materials were buried in the compost (100 g of material for 1200 g of wet compost, 50% water content) and all bioreactors were properly connected, each of the outlet air tubes were connected to their respective water trap. Then, the tubes were plugged to the 40-port Proteus head of a QIC BioStream™ mass spectrometer system (Hyden Analytical). For all bioreactors, partial pressures of oxygen, carbon dioxide, nitrogen, argon and water were recorded periodically.

7-3) Preparation and testing of the compost material

The raw compost (100 kg) of none-sieved organic material was kindly provided by Englobe, St-Rémi, Québec, Canada. **Fig. S37** shows the temperature profile during the successive stages of a typical composting process. The ASTM protocol recommends that the compost be retrieved relatively early in its cooling phase, as it provides the necessary active microbial population needed to run the test. A minimum carbon-to-nitrogen (C/N) ratio of 10 is recommended. The measured carbon-to-nitrogen (C/N) ratio of 12 in the compost from Englobe indicates that this was indeed the case (blue arrow).

Pre-composting tests were performed and their results are reported in **Table S5**. Those tests included: (a) respiration rate via O_2 data acquisition, (b) biochemical parameter determination and (c) C/N ratio. First, the microbial respiration at 20 °C was measured over 2 days for two compost samples, which gave values of 60,1 ± 0.9 mg O_2 per day. The pH, humidity, organic content and C/N ratio were all within the specifications of a suitable compost for ASTM D5338 method.

The right column of **Table S5** shows a pre-composting trial using cellulose powder. The change in C/N ratio from 12 to 20 validated its effective microbial activity.

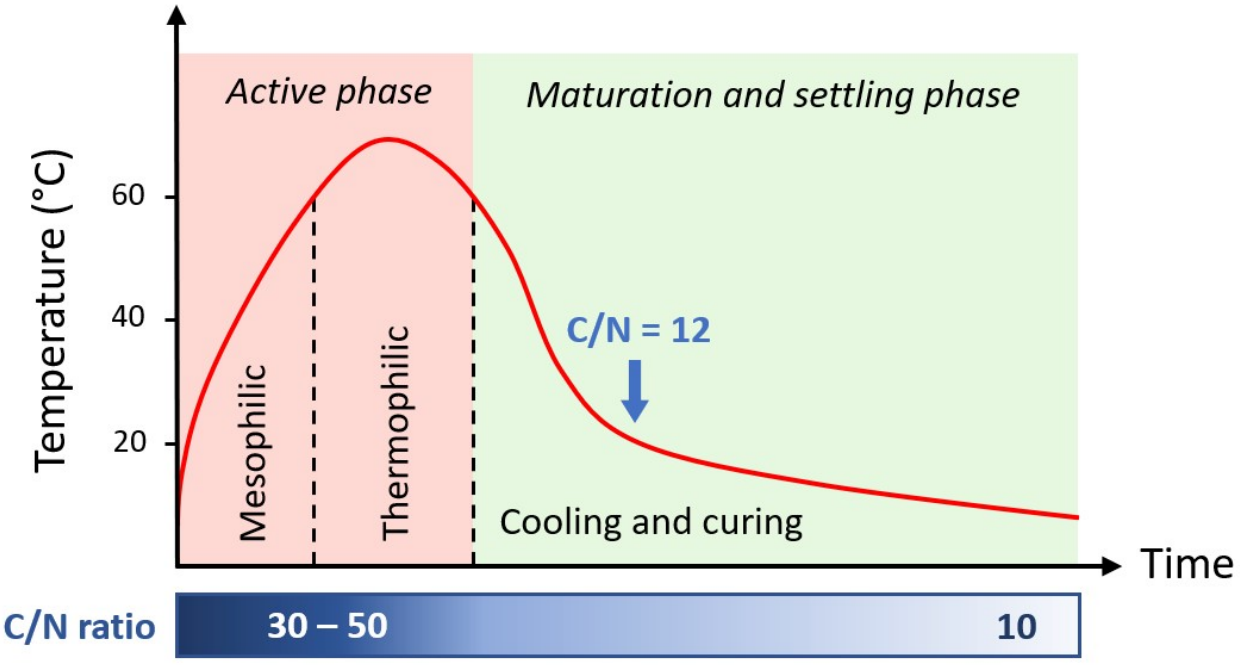

Figure S37 – Typical composting phases and compost selection as per ASTM D5338

Analysis	Compost	Compost + cellulose powder
Respiration rate (mg O_2 per day)	60.1 ± 0.9	-
pH	8.03	7.82
Humidity (%)	46	43
Total dry solids (%)	53.6	56.8
Organic content (%)	30.2	39.3
Total Carbon ($g.kg^{-1}$)	145.2	19.3
Total Nitrogen (Kjeldahl) ($g.kg^{-1}$)	12.1	9.65
C/N ratio	12	20

Table S5 – Results of pre-composting validation tests

7-4) Experimental plan and results

The following materials were used to perform the composting tests: cellulose and sodium alginate powders (Sigma-Aldrich), PLA film, GPE powder and compostable batteries. Each test was performed in triplicate. Each of the 18 reactors was filled with 1.2 kg of wet compost (50 % water content) and the following dry materials (except batteries, which already contained the water in the electrolyte layer):

- Background: no addition
- Cellulose: 100 g
- PLA-D: 95 g
- GPE#3: 95 g
- Na alginate: 100 g
- Batteries: 105 g

The reactors were regularly opened to assess the stage of degradation and mix the materials with the compost. Photographs were taken to document the visual degradation of the materials (**Fig. S38-S40**). After 21 days, most reactors (except for the background) showed the presence of small colonies of fungal mycelium, primarily at the compost surface. Both PLA sheets and batteries were still clearly visible. At the end of the composting tests (63 days), all the reactors except the ones containing PLA sheets seemed to be devoid of remaining material.

The contents of the reactors were poured into platters and close-up pictures were taken (see **Fig. S39**). The composts initially containing GPE#3 and sodium alginate were wet and sticky, likely due to the water-soluble nature of both polymers, whereas the ones containing PLA and batteries were drier and granular. The observation of numerous partially degraded PLA flakes can be explained by the particular biodegradation process of this polymer, which proceeds in two steps starting with a long activation stage, as demonstrated by a composting test clearly showing an acceleration of biodegradation rate

after ca. 40 days (see **Fig. S41** and related discussion). Interestingly, by looking carefully at the degradation images of PLA and batteries, it seems that the battery degradation preceded the degradation of the PLA sheets, with the batteries already broken to pieces after 21 days whereas the PLA sheets were still relatively intact (**Fig. S40**). This suggests that other components in the battery might help the degradation of PLA, since some additives have been reported to accelerate PLA degradation [41-43]. It is therefore possible that the presence of other battery components, such as the conductive carbon layer, have accelerated the first hydrolytic degradation step.

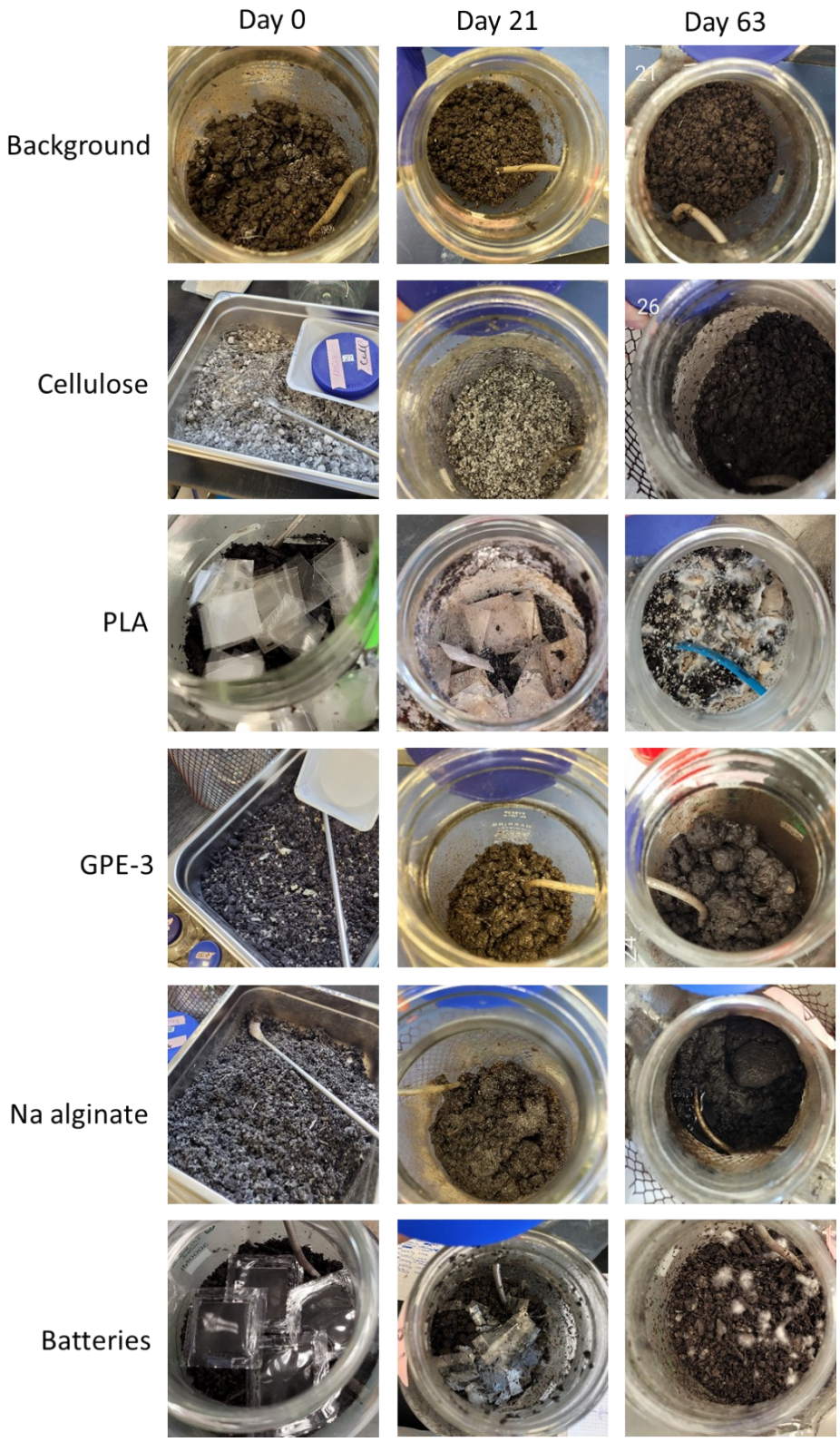

Figure S38 – Pictures of the content of the reactors after 0, 21 and 63 days of composting. One photograph of each triplicate reactors is shown.

Figure S39 – Close-up pictures of the composts from reactors initially containing GPE-3, sodium alginate, PLA and batteries at the end of composting experiment (63 days).

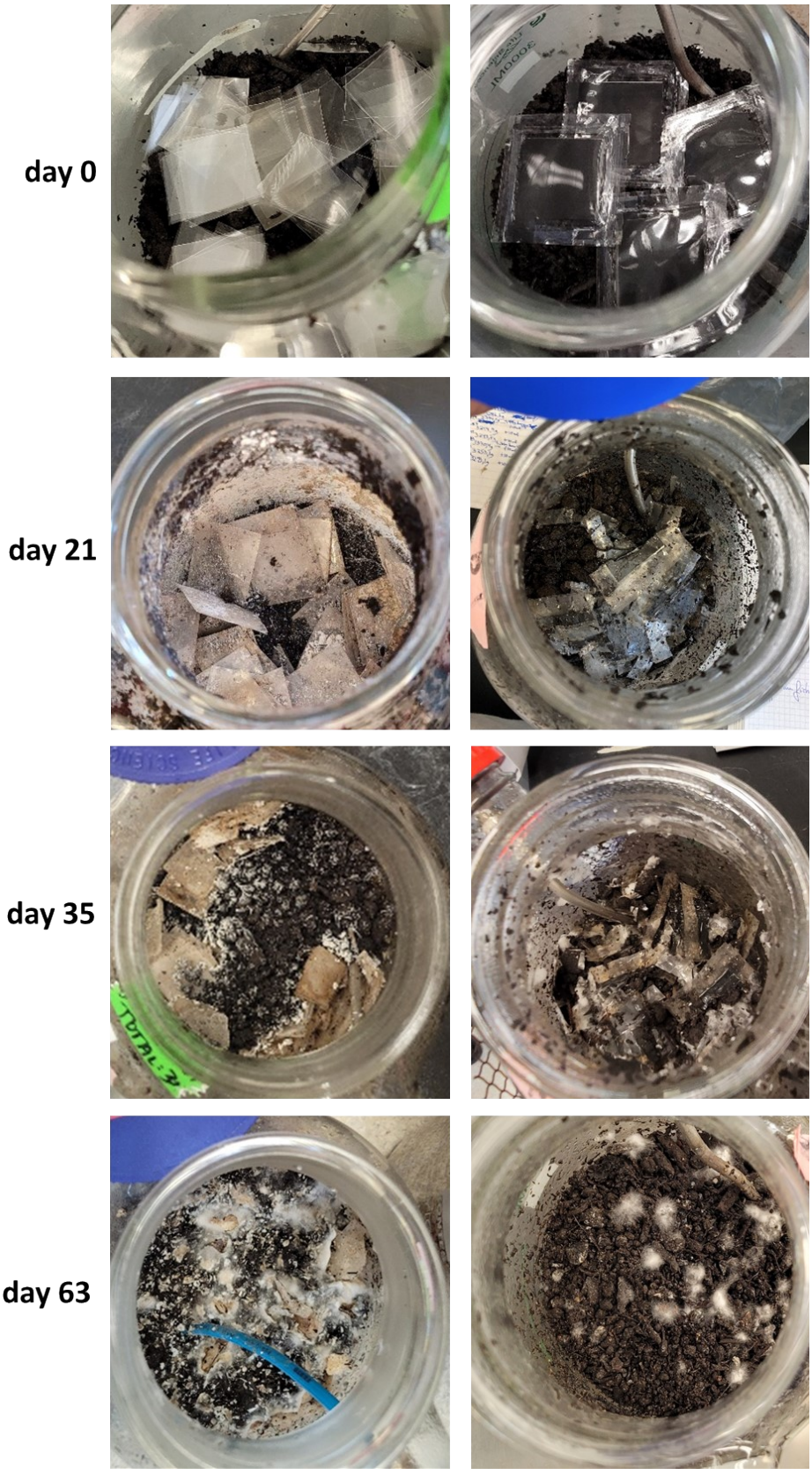

Figure S40 – Reactors containing PLA (left) and batteries (right) after different stages of composting.

Control experiment: long term composting of PLA sheets.

Fig. S41 presents the results of a composting test carried out previously, in similar conditions as the composting test of the battery components (following ASTM D5338 method), where two types of commercial PLA thin films were tested comparatively to cellulose powder (positive reference). The results clearly show that cellulose began to degrade right away, whereas PLA degradation followed a two-stage mechanism, starting with an activation stage of around 40 d. This activation stage has already been reported and explained [44,45]. It involves the hydrolytic degradation of high molecular-weight chains by water, an abiotic process whose duration depends on the polymer crystallinity (the crystalline regions limiting the diffusion of water and enzymes). This first hydrolytic degradation step is mandatory for the microorganisms to be able to use the lower molecular-weight PLA oligomers as a carbon and energy source [46].

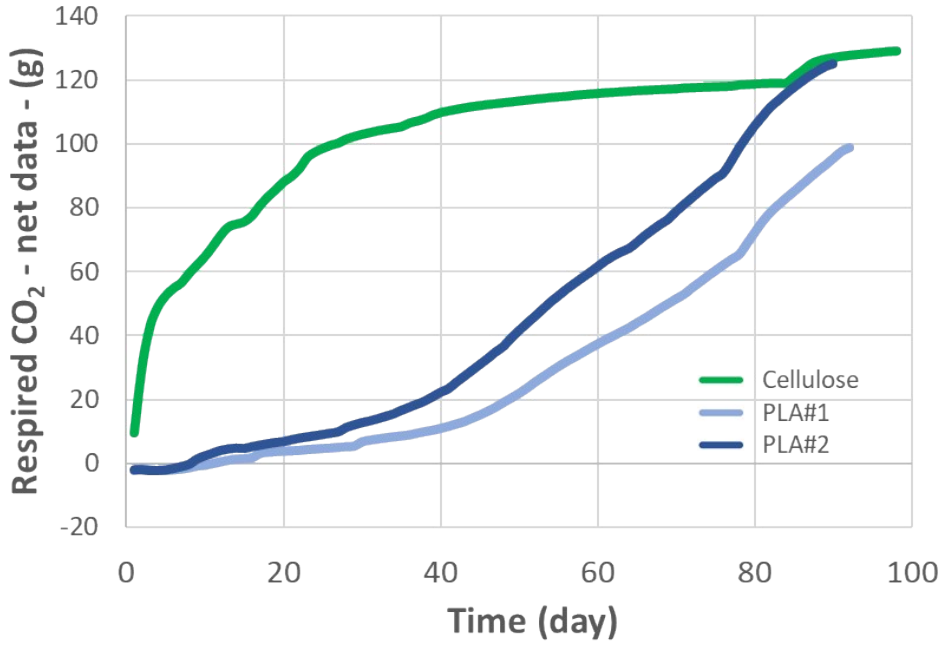

Figure S41 – Long term composting experiment of two commercial PLAs vs. cellulose.

All reactors did not contain the same amount of biodegradable carbon (mineralizable carbon), since each material has a different carbon content. Based on the chemical formula of each component, the mineralizable carbon content was determined and the anticipated CO_2 evolution were calculated for each reactor, as detailed in **Table S6**. Cumulated CO_2 evolution from the reactors is presented in **Fig. S42**.

Material	Formula	Mineralizable carbon content (%)	Content in compost (g)	Anticipated CO_2 evolution (g)
Cellulose	$(C_6H_{10}O_5)_n$	44.4	100	162.8
PLA	$(C_3H_4O_2)_n$	50	95	174.2
Na alginate	$(NaC_6H_7O_6)_n$	36.4	100	133.5
GPE#3	*	49.1	95	171.4
Batteries	-	11.5**	105	44.3

* Estimation of GPE#3 formula based on a 6 wt% PCL content: 24.4 wt% PVAc ($C_4H_2O_6$), 46.3 wt% non-acrylated PVA ($C_2H_4O_1$), 23.2 wt% acrylated PVA ($C_5H_6O_3$), 4.0 wt% non-acrylated PCL ($C_6H_{10}O_2$), and 2.0 wt% acrylated PCL ($C_9H_{12}O_4$).

** Calculation based on the relative weight contents of all battery components.

Table S6 – Calculated mineralizable carbon content and anticipated total CO_2 evolution from biodegradation.

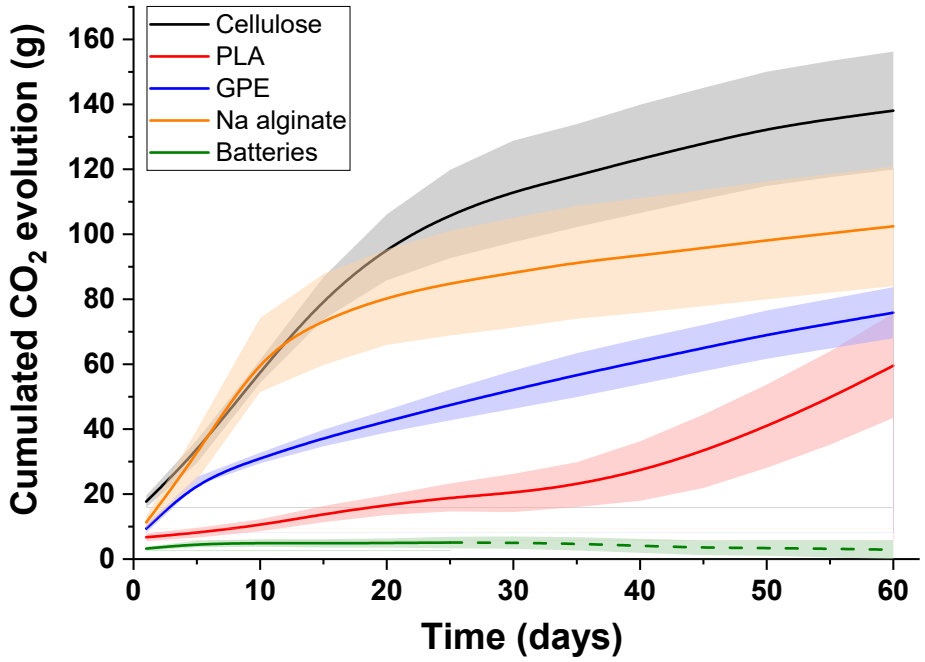

Figure S42 – Accumulated net CO_2 during the composting tests for different materials and batteries (subtracted from the background reference). Note: the dash line part in the Batteries curve shows a negative trend that is not real but demonstrates that the battery composts released less CO_2 than the background compost during this period of time.

7-5) Micro-toxicity bioluminescence test, eco-toxicity tests and elemental analysis

The micro-toxicity bioluminescence test (**Fig. S43a**) is based on the potential of a marine bacteria to produce light, which can be inhibited in the presence of toxic molecules [47]. The toxicity of compost samples can then be evaluated by extracting water-soluble toxic molecules. In the absence of toxic molecules, a low level of light inhibition will be observed, while in the presence of toxic molecules, a high level of light inhibition will be observed. The composts originally containing sodium alginate or batteries showed a light inhibition over 95 %, whereas the other composts showed levels of inhibition below 30 %. This shows a significant toxicity of these composts towards the bacteria.

The eco-toxicity test (**Fig. S43b-c**) was performed according to ASTM standard E1963-22 [48]. Rye seeds (25) were planted in the compost of each reactor at the end of the composting test. The number of germination seeds, as well as the biomass weight produced were determined after 23 days. All composts showed a high level of rye seed germination except the compost originally containing sodium alginate or batteries, which corroborates the results of the bioluminescence test.

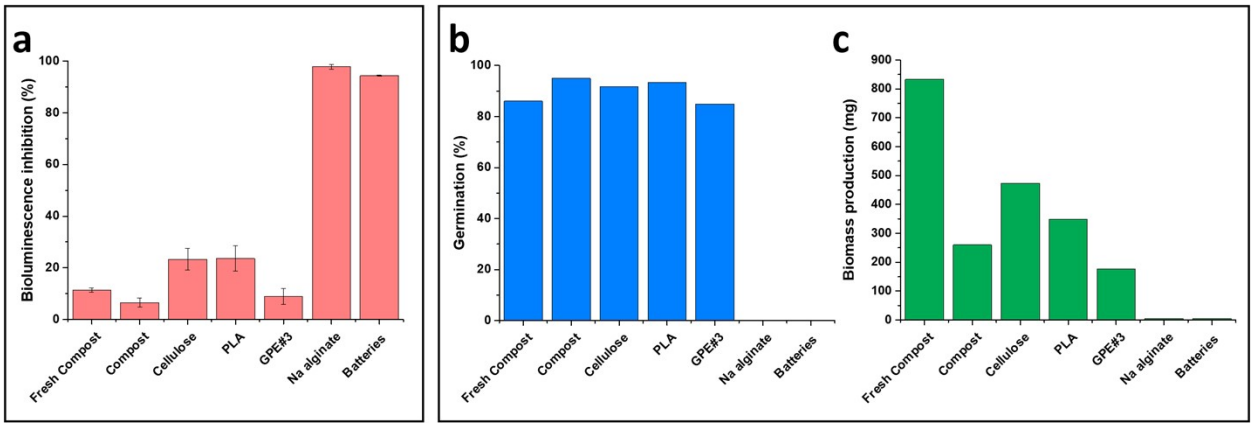

Figure S43 – Micro-toxicity bioluminescence inhibition test (a) and Eco-toxicity tests (b: % of germination of 25 planted rye seeds, c: biomass production).

Analysis		T-0 days	T-63 days					
		Compost 08VEG16	Compost	Cellulose	GPE	Sodium alginate	PLA	Batteries
Humidity	%	47	47	52	47	48	46	46
pH	--	7.9	7.79	7.74	7.92	9.44	7.98	6.14
Carbon total	$mg.kg^{-1}$	149600	127373	142467	166280	134620	152600	160100
Nitrogen total Kjeldahl	$mg.kg^{-1}$	13600	11387	11567	11473	10697	10900	13100
C/N ratio	--	11	11	12	15	13	14	13
Solids total	$g.kg^{-1}$	531	529	481	527	518	535	541
Organic materials	%	28.9	25	28	34	27	31	32
Chlorides	$mg.kg^{-1}$	1650	1527	1610	1993	1077	1490	11955
Ammoniacal nitrogen	$mg.kg^{-1}$	100	184	172	172	256	142	984
Nitrites & nitrates	$mg.kg^{-1}$	170	11	64	<3	<26	4	<26
Sulfates	$mg.kg^{-1}$	703	1613	1068	171	499	827	657
Metal content								
Arsenic	$mg.kg^{-1}$	6.6	7	9	7	7	6	6
Cadmium	$mg.kg^{-1}$	<0.9	<0.9	<0.9	<0.9	<0.9	<0.9	<0.9
Cobalt	$mg.kg^{-1}$	<10	<10	<10	<10	<10	<10	<10
Chromium	$mg.kg^{-1}$	14	16	19	13	15	16	22
Copper	$mg.kg^{-1}$	62	55	65	52	90	53	52
Mercury	$mg.kg^{-1}$	<0.2	<0.2	<0.2	<0.2	<0.2	<0.2	<0.2
Molybdenum	$mg.kg^{-1}$	1.5	2	2	<1.5	2	2	2
Nickel	$mg.kg^{-1}$	12	10	11	10	10	16	13
Lead	$mg.kg^{-1}$	28	28	31	24	32	24	26
Selenium	$mg.kg^{-1}$	<0.5	<0.5	<0.5	<0.5	<0.5	<0.5	<0.5
Zinc	$mg.kg^{-1}$	148	141	157	338	154	172	25283
Silver	$mg.kg^{-1}$	<0.5	<0.5	<0.5	<0.5	<0.5	<0.5	<0.5
Aluminum	$mg.kg^{-1}$	5810	5827	5977	5180	5943	5330	5027
Baryum	$mg.kg^{-1}$	118	134	134	110	145	104	95
Beryllium	$mg.kg^{-1}$	<0.5	<0.5	<0.5	<0.5	<0.5	<0.5	<0.5
Bore	$mg.kg^{-1}$	13	20	20	52	18	16	13
Bismuth	$mg.kg^{-1}$	<10	<10	<10	<10	<10	<10	<10
Calcium	$mg.kg^{-1}$	26100	23167	39133	23600	25100	44633	26383
Iron	$mg.kg^{-1}$	10500	10820	12400	9503	12100	11040	9965
Potassium	$mg.kg^{-1}$	7580	7880	8063	7327	7720	6963	6530
Lithium	$mg.kg^{-1}$	9	7	6	5	7	6	7
Magnesium	$mg.kg^{-1}$	3970	3430	3643	3127	3793	3963	3137
Manganese	$mg.kg^{-1}$	343	358	407	311	380	361	2192
Sodium	$mg.kg^{-1}$	979	742	762	839	12233	805	680
Antimony	$mg.kg^{-1}$	<1	<1	<1	<1	<1	<1	<1
Tin	$mg.kg^{-1}$	<5	<5	5	463	5	<5	46
Strontium	$mg.kg^{-1}$	117	103	184	100	162	262	125
Telluride	$mg.kg^{-1}$	<10	<10	<10	<10	<10	<10	<10
Titanium	$mg.kg^{-1}$	344	246	255	239	270	307	236
Thallium	$mg.kg^{-1}$	<10	<10	<10	<10	<10	<10	<10
Uranium	$mg.kg^{-1}$	<10	<10	<10	<10	<10	<10	<10
Vanadium	$mg.kg^{-1}$	<10	18	17	16	17	17	16

Table S7 – Elemental analysis of the compost before and after the composting tests.

The high tin content in the GPE compost is likely due to the tin (2-ethylhexanoate) catalyst used for the polymerization of caprolactone. The sodium alginate compost shows a high content of sodium (not toxic to plant life) but also a high pH, possibly due to the alginate content. As could be expected, the battery compost shows both a high Zn, Mn, chloride and ammoniacal nitrogen, coming from the electrodes and electrolyte salts.

7-6) Microbial community genetic analysis

Experimental details

Compost samples were collected before testing (T0) and after 49 days (T49), and stored at -80 °C until DNA extraction. The samples were extracted using the PowerSoil Max DNA extraction kit (cat#12988-10, QIAgen). Samples (10 g) were weighed and transferred to a PowerMax bead tube containing 15 mL of PowerBead solution. Nucleic acid elution was done with 3 mL of DNAse-free Ambion water. DNA extraction was performed using NucleoMag NGS Clean-up and Size Select beads (cat# MN-744970, Macherey-Nagel) in a 1:1 (v:v) ratio. Then precipitation was performed to concentrate the nucleic acids. The final extracted gDNA was quantified using the Qubit dsDNA HS assay kit (cat# Q32854, ThermoFisher Scientific).

16S and ITS Sequencing Library Preparation. The preparation of the 16S and the ITS libraries was done following the Illumina's guide named "16S Metagenomic Sequencing Library Preparation". The two pairs of primers used are as follow:

- (16S): TCGTCGGCAGCGTCAGATGTGTATAAGAGACAGGTGYCAGCMGCCGCGGTAA and GTCTCGTGGGCTCGGAGATGTGTATAAGAGACAGCCGYCAATTYMTTTRAGTTT;
- (ITS): TCGTCGGCAGCGTCAGATGTGTATAAGAGACAGGAACGCAGCRAAIIGYGA and GTCTCGTGGGCTCGGAGATGTGTATAAGA GACAGTCCTCCGCTTATTGATATGC.

The purification of the amplicons was done using the NucleoMag NGS Clean-up and Size beads Select (cat# MN-744970, Macherey-Nagel) instead of AmpureXP beads. An equimolar pool of all the 24 16S and 23 ITS (one sample, R32_BATT_49_OCT22_B_MIX, did not amplify) libraries were prepared and quantified using a TapeStation System and a HS DNA kit (cat# 5067-5592, Agilent).

Libraries sequencing on MiSeq. A paired-end sequencing (2 × 250 bp) of the 16S and ITS amplicon pools was carried out on an Illumina MiSeq sequencer, using the MiSeq Reagent kit V2, 500 cycles (cat# MS-102-2003, Illumina). For the analysis of fungal communities, a pool of 23 ITS libraries was generated from the amplification of the ITS2 region and was sequenced. For the analysis of bacterial communities, a pool of 24 16S rRNA libraries was generated from the amplification of the eubacteria and archaebacteria V4-V5 regions and was sequenced.

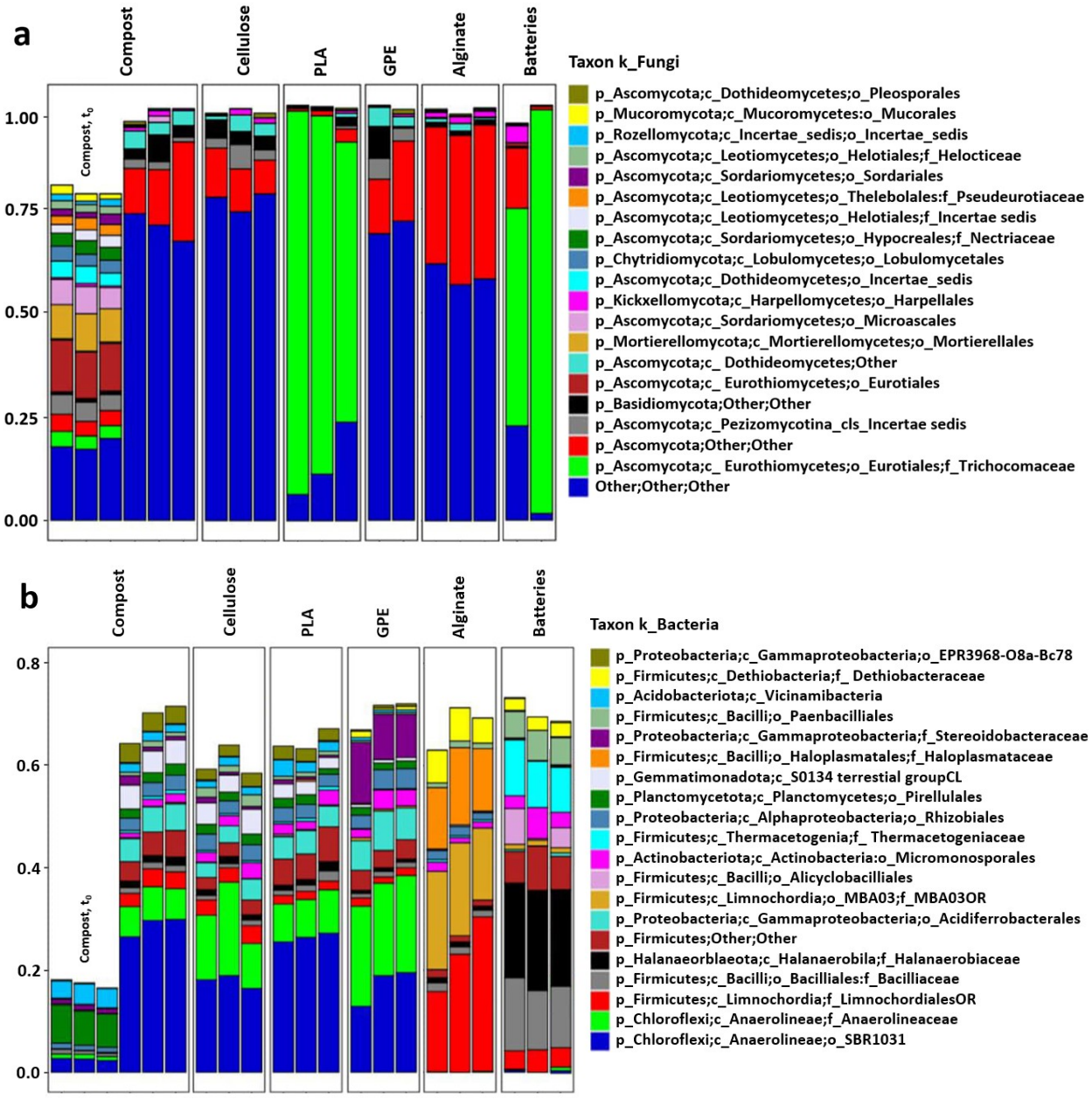

Figure S44 – Taxonomic profiles of the microbial populations at the family level, before and after the composting tests; a) Taxonomic profile of the fungi communities; b) Taxonomic profile of the bacteria communities. The 20 most abundant bacterial families are displayed. Data represents the relative abundance of reads for a taxonomic group

Analysis of the taxonomic profiles

Fungal community analysis via ITS rRNA sequencing (**Fig. S44a**)

A global loss of biodiversity was observed in the fungal populations during the composting test, which can be associated with the particular conditions that were kept in the reactors (58 °C, 50 % water content). However, after 49 days the fungi evolved quite similarly in the background, cellulose, GPE and SA composts. On the other hand, the PLA and battery composts evolved very differently, with a strong expansion of the *Trichocomaceae* family, a type of fungi associated with PLA degradation [49,50] that are known for their active colonization strategies [51,52]. These relatively common fungi are able to grow long strains of mycelium to colonize surfaces. **Fig. S45** displays SEM pictures showing such strings of mycelium grown on top of PLA sheets via chemotropism.

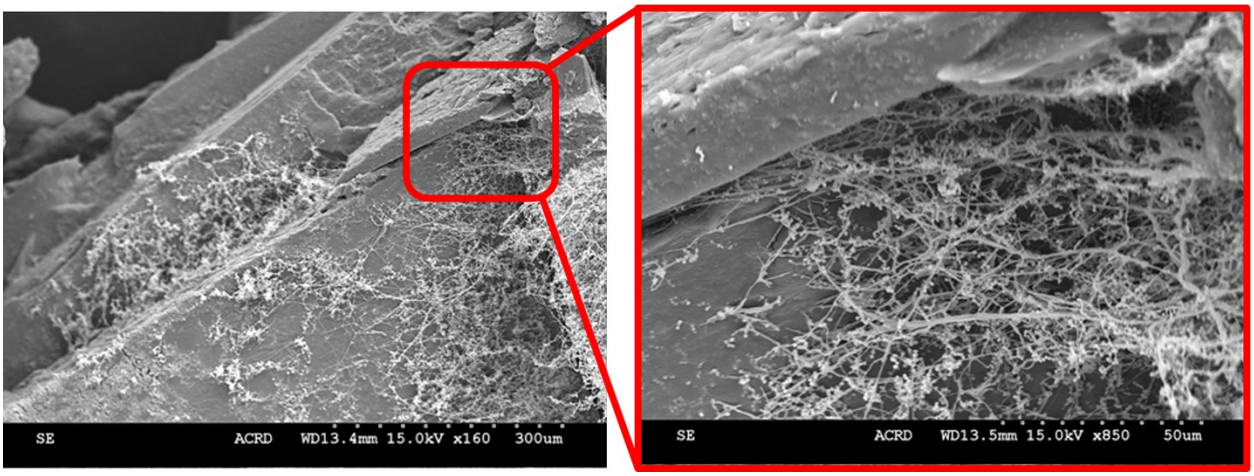

Figure S45 – SEM images showing fungi mycelium colonizing polymer sheets in the PLA compost.

Bacterial community analysis via 16S rRNA sequencing (**Fig. S44b**).

The 16S taxonomy in the three T0 background compost samples (initial point) was relatively different from the T49 compost samples (after 49 days), which shows that a wide bacterial diversity developed in the compost during the timeframe of the experiment. At T49, the populations of the background compost, cellulose, PLA and GPE composts were very similar, with a huge proportion of *Anaerolineaceae* family (deep blue and light green). The GPE compost showed an enhanced presence of the *Steroidobacteraceae* family (deep violet), a family of bacteria that has been identified in the biodegradation of PVA [53]. On the other hand, the bacterial communities of the alginate and battery composts evolved quite differently. The alginate compost showed the predominant presence of bacteria from the *Haloplasmataceae* family (orange, *Bacilli* class), *Limnochordia* class (beige and red) and *Dethiobacteraceae* class (yellow), whereas the battery compost showed a significant presence of the *Thermacetogeniaceae, Bacillaceae* and *Halanaerobiaceae* families (light blue, grey and black), which constitute less than 1% of the communities of the other composts.

Discussion on the genetic analysis of the alginate and battery composts

The bacterial communities evolved in a particular way in the SA compost, with communities from the *Limnochordia* class largely dominating. This class of bacteria is specialized in the degradation of cellulosic materials [54-56], and might have been more resistant than other species to the high pH progressively building in the compost. Their presence explains why the SA could be totally converted into CO_2 despite the toxic conditions.

The battery compost showed a distinctive evolution of the microbial communities compared to all other composts. It showed a significant development of certain types of bacteria and fungi families. Even though it is difficult to establish the reasons for such evolutions from a single study, some interesting information can be highlighted:

- We could observe a similar development of the fungi from battery and PLA composts, with the development of the *Trichocomaceae* family. This is likely due to the fact that PLA is the first material encountered by the microorganisms.
- The bacterial communities of the battery compost also evolved in a unique way, with the development of bacteria that didn't or scarcely develop in the other composts: mainly *Bacillaceae*, *Thermacetogeniaceae* and *Halanaerobiaceae*, but also *Dethiobacteraceae* (also present in the SA compost). *Bacillaceae* are a family of highly resistant aerobic bacteria, found in multiple locations and environments, able to survive in high salt concentrations [57], and are known to be able to degrade various polymer chains [58]. Bacteria of the *Halanaerobiaceae* and *Dethiobacteriaceae* families have also been demonstrated to sustain highly salted environments [59-61].
- Some of these bacteria families, grown in significant quantities in the compost, have also been shown to be able to convert CO_2 into methane (*Thermacetogeniaceae)* [62,63] or acetate (*Halanaerobiaceae*) [64]. This might (at least partially) explain the lack of CO_2 evolution during the composting process.

References

[1] S. Gulliani, M. Volpe, A. Messineo and R. Volpe, RSC Sustainability, 2023, 1, 1085-1108.

[2] R. Hamade, R. Al Ayache, M. Bou Ghanem, S. El Masri, A. Ammouri, Procedia Manufacturing, 2020, 43, 415–422

[3] C. Coker, *BioCycle*, **2021,** https://www.biocycle.net/spontaneous-combustion-in-composting-the-causes/.

[4] U. Rojas-Alva, L. Mancini, A. M. Pranji, E. Marini, B. Bozzini, *Process Safety and Environmental Protection*, **2025**, 199, 107175.

[5] L. Yin, X. Huang, H. Xu, Y. Zhang, J. Lam, J. Cheng and J. A. Rogers*, Advanced Materials*, 2014, **26**, 3879-3884.

[6] M. H. Lee, J. Lee, S.-K. Jung, D. Kang, M. S. Park, G. D. Cha, K. W. Cho, J.-H. Song, S. Moon, Y. S. Yun, S. J. Kim, Y. W. Lim, D.-H. Kim and K. Kang, *Advanced Materials*, 2021, **33**, 2004902.

[7] A. Poulin, X. Aeby and G. Nyström, *Scientific Reports*, 2022, **12**, 11919.

[8] M. Karami-Mosammam, D. Danninger, D. Schiller and M. Kaltenbrunner, *Advanced Materials*, 2022, **34**, 2204457.

[9] P. Yang, J. Li, S. W. Lee and H. J. Fan, *Advanced Science*, 2022, **9**, 2103894.

[10] M. Navarro-Segarra, C. Tortosa, C. Ruiz-Díez, D. Desmaële, T. Gea Raquel Barrena, N. Sabaté and J. P. Esquivel, *Energy & Environmental Science*, 2022, **15**, 2900-2915.

[11] M. Navarro-Segarra, O. A. Ibrahim, I. Martin-Fernandez, C. Tortosa, J. M. Ormaetxea, M. Baumann, M. Weil and J. P. Esquivel, *Energy & Environmental Science*, 2024, **17**, 5639-5652.

[12] Celplast metallized PLA webpage, https://www.celplast.com/family/enviromet/

[13] Jung, Y. H., Zhang, H., Gong, S. & Ma, Z. High-performance green semiconductor devices: materials, designs, and fabrication. Semiconductor Science and Technology 32, 063002 (2017). https://doi.org:/10.1088/1361-6641/aa6f88

[14] Zheng, Q. et al. Biodegradable triboelectric nanogenerator as a life-time designed implantable power source. Science Advances 2, e1501478 (2016). https://doi.org:/10.1126/sciadv.1501478

[15] Fu, K. K., Wang, Z., Dai, J., Carter, M. & Hu, L. Transient Electronics: Materials and Devices. Chemistry of Materials 28, 3527-3539 (2016). https://doi.org:/10.1021/acs.chemmater.5b04931

[16] Huang, X. et al. A Fully Biodegradable Battery for Self-Powered Transient Implants. Small 14, 1800994 (2018). https://doi.org:/10.1002/smll.201800994

[17] Edgar, K. J. et al. Advances in cellulose ester performance and application. Progress in Polymer Science 26, 1605-1688 (2001). https://doi.org:/10.1016/S0079-6700(01)00027-2

[18] Grant, G. T., Morris, E. R., Rees, D. A., Smith, P. J. C. & Thom, D. Biological interactions between polysaccharides and divalent cations: The egg-box model. FEBS Letters 32, 195-198 (1973). https://doi.org:/10.1016/0014-5793(73)80770-7

[19] Braccini, I. & Pérez, S. Molecular Basis of Ca2+-Induced Gelation in Alginates and Pectins: The Egg-Box Model Revisited. Biomacromolecules 2, 1089-1096 (2001). https://doi.org:/10.1021/bm010008g

[20] Phillips, C., Al-Ahmadi, A., Potts, S.-J., Claypole, T. & Deganello, D. The effect of graphite and carbon black ratios on conductive ink performance. Journal of Materials Science 52, 9520-9530 (2017). https://doi.org:/10.1007/s10853-017-1114-6

[21] Decker, C. & Jenkins, A. D. Kinetic approach of oxygen inhibition in ultraviolet- and laser-induced polymerizations. Macromolecules 18, 1241-1244 (1985). https://doi.org:/10.1021/ma00148a034

[22] Studer, K., Decker, C., Beck, E. & Schwalm, R. Overcoming oxygen inhibition in UV-curing of acrylate coatings by carbon dioxide inerting, Part I. Progress in Organic Coatings 48, 92-100 (2003). https://doi.org:/10.1016/S0300-9440(03)00120-6/

[23] Belon, C., Allonas, X., Croutxé-barghorn, C. & Lalevée, J. Overcoming the oxygen inhibition in the photopolymerization of acrylates: A study of the beneficial effect of triphenylphosphine. Journal of Polymer Science Part A: Polymer Chemistry 48, 2462-2469 (2010). https://doi.org:/10.1002/pola.24017

[24] Chopra, N., Abraham, B. E., McGuire, G., Black, R. & Laforgue, A. Printable ultra-violet light emitting diode curable electrolyte for thin-film batteries US patent 2022/0149390 (2022).

[25] Patil, R. S., Thomas, J., Patil, M. & John, J. To Shed Light on the UV Curable Coating Technology: Current State of the Art and Perspectives. Journal of Composites Science 7 (2023).

[26] Della Monica, M., Ceglie, A. & Agostiano, A. A conductivity equation for concentrated aqueous solutions. Electrochimica Acta 29, 933-937 (1984). https://doi.org:/10.1016/0013-4686(84)87138-8

[27] Bettinger, C. J. Biodegradable Elastomers for Tissue Engineering and Cell–Biomaterial Interactions. Macromolecular Bioscience 11, 467-482 (2011). https://doi.org:/10.1002/mabi.201000397

[28] Shan, A. H., Jiang, L. & Li, Z. Biodegradable Polyester Thermogelling System as Emerging Materials for Therapeutic Applications. Macromolecular Materials and Engineering 303, 1700656 (2018). https://doi.org:/10.1002/mame.201700656

[29] van Bochove, B. & Grijpma, D. W. Photo-crosslinked synthetic biodegradable polymer networks for biomedical applications. Journal of Biomaterials Science, Polymer Edition 30, 77-106 (2019). https://doi.org:/10.1080/09205063.2018.1553105

[30] Xu, C., Lee, W., Dai, G. & Hong, Y. Highly Elastic Biodegradable Single-Network Hydrogel for Cell Printing. ACS Applied Materials & Interfaces 10, 9969-9979 (2018). https://doi.org:/10.1021/acsami.8b01294

[31] Suhaimi, N., Syed, M. A., Shamaan, N. A. & Othman, A. R. Biodegradation of PEGs: A review. Journal of Biochemistry, Microbiology and Biotechnology 9, 1-18 (2021). https://doi.org:/10.54987/jobimb.v9i1.569

[32] Gross, R. A. & Kalra, B. Biodegradable Polymers for the Environment. Science 297, 803-807 (2002). https://doi.org:/10.1126/science.297.5582.803

[33] Braam, K. & Subramanian, V. A Stencil Printed, High Energy Density Silver Oxide Battery Using a Novel Photopolymerizable Poly(acrylic acid) Separator. Advanced Materials 27, 689-694 (2015). https://doi.org:/10.1002/adma.201404149

[34] Charkoudian, J. C. Method for reducing zinc oxide content of zinc particles. US patent US4006036 (1974).

[35] Friess, R. The reactions of ammonia on the system ZnCl2-NH4Cl-H2O. Journal of the American Chemical Society 52, 3083-3087 (1930). https://doi.org:/10.1021/ja01371a007

[36] Bredland, A. M. & Hull, M. N. Leclanché Electrolyte Compositional Studies for Thin Film Batteries. Journal of The Electrochemical Society 123, 311 (1976). https://doi.org:/10.1149/1.2132816

[37] Larcin, J., Maskell, W. C. & Tye, F. L. Leclanché cell investigations I: Zn(NH3)2Cl2 solubility and the formation of ZnCl2·4Zn(OH)2·H2O. Electrochimica Acta 42, 2649-2658 (1997). https://doi.org:/10.1016/S0013-4686(96)00456-2

[38] Thomas Goh, F. W. et al. A Near-Neutral Chloride Electrolyte for Electrically Rechargeable Zinc-Air Batteries. Journal of The Electrochemical Society 161, A2080 (2014). https://doi.org:/10.1149/2.0311414jes

[39] Clark, S. et al. Towards rechargeable zinc–air batteries with aqueous chloride electrolytes. Journal of Materials Chemistry A 7, 11387-11399 (2019). https://doi.org:/10.1039/C9TA01190K

[40] Brodd, R. J. & DeWane, H. J. Impedance of Leclanche Cells and Batteries. Journal of The Electrochemical Society 110, 1091 (1963). https://doi.org:/10.1149/1.2425596

[41] Turco, R. et al. Biocomposites based on Poly(lactic acid), Cynara Cardunculus seed oil and fibrous presscake: a novel eco-friendly approach to hasten PLA biodegradation in common soil. Polymer Degradation and Stability 188, 109576 (2021). https://doi.org:/10.1016/j.polymdegradstab.2021.109576

[42] Kamaludin, N. H. I., Ismail, H., Rusli, A., Sam, S. T. & Osman, H. Evaluation and Enhancement of Polylactic Acid Biodegradability in Soil by Blending with Chitosan. Journal of Polymers and the Environment 31, 2727-2740 (2023). https://doi.org:/10.1007/s10924-023-02762-9

[43] Liparoti, S., Iozzino, V., Speranza, V. & Pantani, R. Modulating poly(lactic acid) degradation rate for environmentally sustainable applications. Waste Management 175, 215-224 (2024). https://doi.org:/10.1016/j.wasman.2024.01.004

[44] Castro-Aguirre, E., Iñiguez-Franco, F., Samsudin, H., Fang, X. & Auras, R. Poly(lactic acid)—Mass production, processing, industrial applications, and end of life. Advanced Drug Delivery Reviews 107, 333-366 (2016). https://doi.org:/10.1016/j.addr.2016.03.010

[45] Karamanlioglu, M., Preziosi, R. & Robson, G. D. Abiotic and biotic environmental degradation of the bioplastic polymer poly(lactic acid): A review. Polymer Degradation and Stability 137, 122-130 (2017). https://doi.org:/10.1016/j.polymdegradstab.2017.01.009

[46] Lunt, J. Large-scale production, properties and commercial applications of polylactic acid polymers. Polymer Degradation and Stability 59, 145-152 (1998). https://doi.org:/10.1016/S0141-3910(97)00148-1

[47] Scroggins, R. P., Sergy, G., Sprague, J. B. & McLeay, D. J. Biological Test Method: Toxicity Test Using Luminescent Bacteria. Environment Canada, 1992 https://publications.gc.ca/site/eng/9.579452/publication.html

[48] Standard Guide for Conducting Terrestrial Plant Toxicity Tests. ASTM E1963-22 (2022). https://doi.org:/10.1520/E1963-22

[49] Moore-Kucera, J. et al. Native soil fungi associated with compostable plastics in three contrasting agricultural settings. Applied Microbiology and Biotechnology 98, 6467-6485 (2014). https://doi.org:/10.1007/s00253-014-5711-x

[50] Satti, S. M., Shah, A. A., Auras, R. & Marsh, T. L. Isolation and characterization of bacteria capable of degrading poly(lactic acid) at ambient temperature. Polymer Degradation and Stability 144, 392-400 (2017). https://doi.org:/10.1016/j.polymdegradstab.2017.08.023

[51] Egbuta, M. A., Mwanza, M. & Babalola, O. O. A Review of the Ubiquity of Ascomycetes Filamentous Fungi in Relation to Their Economic and Medical Importance. Advances in Microbiology 6, 1140-1158 (2016). https://doi.org:/10.4236/aim.2016.614103

[52] Houbraken, J. & Samson, R. A. Phylogeny of Penicillium and the segregation of Trichocomaceae into three families. Studies in Mycology 70, 1-51 (2011). https://doi.org:/10.3114/sim.2011.70.01

[53] Nogi, Y., Yoshizumi, M., Hamana, K., Miyazaki, M. & Horikoshi, K. Povalibacter uvarum gen. nov., sp. nov., a polyvinyl-alcohol-degrading bacterium isolated from grapes. International Journal of Systematic and Evolutionary Microbiology 64, 2712-2717 (2014). https://doi.org:https://doi.org/10.1099/ijs.0.062620-0

[54] Liu, H. et al. Degradation of lignocelluloses in straw using AC-1, a thermophilic composite microbial system. PeerJ 9, 1-13 (2021).

[55] Karnachuk, O. V. et al. Novel thermophilic genera Geochorda gen. nov. and Carboxydochorda gen. nov. from the deep terrestrial subsurface reveal the ecophysiological diversity in the class Limnochordia. Frontiers in Microbiology 15 (2024). https://doi.org:/10.3389/fmicb.2024.1441865

[56] Nguyen, T. V., Trinh, H. P. & Park, H.-D. Genome-based analysis reveals niche differentiation among Firmicutes in full-scale anaerobic digestion systems. Bioresource Technology 418, 131993 (2025). https://doi.org:/10.1016/j.biortech.2024.131993

[57] Oren, A. Novel insights into the diversity of halophilic microorganisms and their functioning in hypersaline ecosystems. npj Biodiversity 3, 18 (2024). https://doi.org:/10.1038/s44185-024-00050-w

[58] Mandic-Mulec, I., Stefanic, P. & van Elsas Jan, D. Ecology of Bacillaceae. Microbiology Spectrum 3, 10.1128/microbiolspec.tbs-0017-2013 (2015). https://doi.org:/10.1128/microbiolspec.tbs-0017-2013

[59] Sorokin, D. Y., Tourova, T. P., Mußmann, M. & Muyzer, G. Dethiobacter alkaliphilus gen. nov. sp. nov., and Desulfurivibrio alkaliphilus gen. nov. sp. nov.: two novel representatives of reductive sulfur cycle from soda lakes. Extremophiles 12, 431-439 (2008). https://doi.org:/10.1007/s00792-008-0148-8

[60] Ivanova, N. et al. Complete genome sequence of the extremely halophilic Halanaerobium praevalens type strain (GSLT). Standards in Genomic Sciences 4, 312-321 (2011). https://doi.org:/10.4056/sigs.1824509

[61] Oren, A. Life at high salt concentrations, intracellular KCl concentrations, and acidic proteomes. Frontiers in Microbiology 4 (2013). https://doi.org:/10.3389/fmicb.2013.00315

[62] Hattori, S., Kamagata, Y., Hanada, S. & Shoun, H. Thermacetogenium phaeum gen. nov., sp. nov., a strictly anaerobic, thermophilic, syntrophic acetate-oxidizing bacterium. International Journal of Systematic and Evolutionary Microbiology 50, 1601-1609 (2000). https://doi.org:/10.1099/00207713-50-4-1601

[63] Keller, A., Schink, B. & Müller, N. Energy-Conserving Enzyme Systems Active During Syntrophic Acetate Oxidation in the Thermophilic Bacterium Thermacetogenium phaeum. Frontiers in Microbiology 10 (2019). https://doi.org:/10.3389/fmicb.2019.02785

[64] Vavourakis, C. D. et al. A metagenomics roadmap to the uncultured genome diversity in hypersaline soda lake sediments. Microbiome 6, 168 (2018). https://doi.org:/10.1186/s40168-018-0548-7